

PROJECT GNOME

THE ENVIRONMENT CREATED BY A NUCLEAR
EXPLOSION IN SALT

D. Rawson
C. Boardman
N. Jaffe-Chazan

Lawrence Radiation Laboratory
University of California
Livermore, California

September 1964

This document is
PUBLICLY RELEASABLE

B Steele
Authorizing Official
Date: 5-9-06

DISCLAIMER

This report was prepared as an account of work sponsored by an agency of the United States Government. Neither the United States Government nor any agency Thereof, nor any of their employees, makes any warranty, express or implied, or assumes any legal liability or responsibility for the accuracy, completeness, or usefulness of any information, apparatus, product, or process disclosed, or represents that its use would not infringe privately owned rights. Reference herein to any specific commercial product, process, or service by trade name, trademark, manufacturer, or otherwise does not necessarily constitute or imply its endorsement, recommendation, or favoring by the United States Government or any agency thereof. The views and opinions of authors expressed herein do not necessarily state or reflect those of the United States Government or any agency thereof.

DISCLAIMER

Portions of this document may be illegible in electronic image products. Images are produced from the best available original document.

CONTENTS

ABSTRACT	5
ACKNOWLEDGMENTS	7
CHAPTER 1 INTRODUCTION	8
1.1 Background	8
1.2 Objectives	10
1.3 Exploration Phases	13
1.4 Observations Immediately Following the Explosion	13
CHAPTER 2 THE CAVITY ENVIRONMENT	15
2.1 General	15
2.2 Cavity Volume and Shape	17
2.3 Rubble and Associated Radioactive Melt	20
2.4 Rock Temperatures	27
CHAPTER 3 PERMANENT DISPLACEMENTS	30
3.1 General	30
3.2 Displacements Surrounding the Cavity	31
3.3 Implications of Localized Uplift Between the Cavity and the Ground Surface	33
3.4 Summary of Cavity Radii and Implications About "Blow-off" of the Cavity Walls	37
CHAPTER 4 FRACTURING AND DIFFERENTIAL ROCK MOTIONS	39
4.1 Local Uplift of Strata Over the Shot Point	39
4.2 Melt and Gas Injected from the Cavity into Fractures	41
4.3 Deformation Surrounding the Cavity	47
4.4 Deformation of the Preshot Emplacement Drift	51
CHAPTER 5 VENTING	57
5.1 The Venting Process	57
5.2 The Vent Path Environment	59
CHAPTER 6 AN INTERPRETATION OF THE EXPLOSION DYNAMICS	67
APPENDIX A DESCRIPTION OF ROCK STRATA SUR- ROUNDING THE GNOME EVENT	75
APPENDIX B APPROXIMATE PRESHOT CHEMICAL COMPOSITION OF THE ROCK FUSED AND VAPORIZED BY THE GNOME EVENT	78

CONTENTS (Continued)

APPENDIX C	ASSUMPTIONS INHERENT IN THE TREATMENT OF THE PERMANENT DISPLACEMENT DATA	79
APPENDIX D	CAVITY VOID, RUBBLE, AND MELT VOLUME CALCULATIONS	80
APPENDIX E	RUBBLE DISTRIBUTION	83
REFERENCES	73
TABLES		
3.1	Theoretical and Final Cavity Radii Comparison	37
FIGURES		
1.1	Vertical section through the Gnome postshot environment	9
1.2	Plan view showing the post-explosion exploration and cavity	11
2.1	Gnome cavity: reflected ceiling plan	16
2.2	Cavity profile A-A'	18
2.3	Cavity profiles B-B' and C-C'	19
2.4	Schematic sections through the Gnome cavity showing approximate distribution of radio- activity two years after the explosion	22
2.5	Typical melt samples from underground drill holes	26
2.6	Temperature vs radial distance from working point six months after the detonation	28
3.1	Permanent rock displacement vs distance from working point	31
3.2	Vertical section showing configuration of localized uplift	36
4.1	Map of Gnome ground surface showing fractures and approximate boundary of uplifted region	39
4.2	Profiles of the Gnome ground-surface permanent displacements showing the uplifted region configuration	40
4.3	Rock deformation revealed by postshot mining - plan view	43
4.4	Vertical section H-H'' showing deformation at end of hole # 12 drift	45
4.5	Displacement of underground instrument and shock-study sample holes - plan view	46
4.6	Typical faults produced by the explosion	49

CONTENTS (Continued)

4.7	Plan schematic of trellis fracture pattern associated with deformation along the line-of-sight emplacement drift	50
4.8	Vertical section E-E' showing partial closure of preshot emplacement drift	51
4.9	Vertical sections F-F' and G-G' showing closure of "buttonhook drift"	53
4.10	Intrusive melt breccia	55
5.1	Deformation of emplacement drift near shaft	61
5.2	Deformation of emplacement drift between shaft and cavity	63
5.3	Vent path	65
5.4	View of interior of the Gnome cavity. Note size of man	66
6.1	Schematic vertical sections showing cavity development	69

ABSTRACT

The Gnome event, a 3.1 ± 0.5 kiloton nuclear explosion, was conducted at a depth of 361 m in bedded rock salt near Carlsbad, New Mexico. ^{1/} ~~This explosion~~ ^{The burst} melted approximately 3.2×10^6 kilograms of rock salt and produced a standing cavity with a volume of about 27,200 cubic meters. ^{2/} The cavity has a pronounced bulge at its equator. The development of this asymmetry was controlled by the preshot character of the rock: horizontal weaknesses in the form of bedding planes and clay layers. ^{2/} The molten salt mixed with the condensing radioactive debris and about 11.6×10^6 kg of rock from the cavity walls, to form a radioactive "puddle" of melt and rock breccia at the base of the cavity. This zone is blanketed by about 13.6×10^6 kg of rubble that resulted primarily from ceiling collapse, thus shielding the "puddle" so that when personnel entered the cavity, gamma radiation levels were rarely in excess of 20 mR/hr. ^{3/}

During the dynamic cavity growth period of about 100 msec, radial cracks propagated closely behind the outgoing compressional shock wave. ^{3/} Molten rock had not yet mixed well with vaporized fission products and consequently melt injected into these cracks was not radioactive or only slightly so. ^{1/} ~~The maximum observed~~ ^{11 references. and} extent of these fractures, measured from the center of the explosion, is 40 m laterally, 38 m above and 25 m below.

Leakage of radioactive gases through the rock is detectable by the presence of radiation damaged salt. Generally, there was no evidence of leakage beyond 40 m and the maximum observed extent at 65.5 m is thought to be associated with fracturing to a natural cavity.

Close-in stemming failed and cavity gases vented dynamically into the emplacement drift. Back-up stemming confined the dynamic venting but allowed the low pressure release of steam and gaseous fission products. The formation of radial cracks and bedding plan partings, coupled with the emplacement configuration to accommodate a neutron-physics experiment, caused the stemming failure.

Asymmetry of rock displacements, fractures observed, and the permanent surface displacements indicate localized uplift of the rock between the cavity and the ground surface. It is interpreted that this uplift was caused by spall of the upper few hundred feet of rock which momentarily decreased the overburden pressure. The cavity pressure then exceeded overburden pressure and the cavity expanded preferentially upwards.

A zone of increased permeability was defined to extend at least 46 m laterally and 105 m above the point of the explosion. The permeability increase was established by complete circulation loss of the drill fluid and is primarily associated with motions and partings along bedding planes - the major preshot weakness in the rock.

ACKNOWLEDGMENTS

The authors gratefully acknowledge the encouragement and criticism of Dr. Gary H. Higgins and Dr. Philip Randolph. The close support of John Brewer and Lyn Ballou aided greatly in accomplishing the exploration. We would also like to thank the many personnel of Reynolds Engineering and Electric Company for their drilling, mining, and hazards-control participation during the exploration; Holmes and Narver, Inc., for survey control; Boyles Bros., Shaffer Tool Works, and Moran Bros. for their drilling accomplishments. For the excellent photographic coverage we acknowledge Ray Jaeger and the Lawrence Radiation Laboratory Graphic Arts staff.

CHAPTER 1

INTRODUCTION

1.1 BACKGROUND

Project Gnome was the first scientific experiment with nuclear explosives designed to provide information pertaining to the non-military uses of these explosives. A 3.1 ± 0.5 kt nuclear device was detonated at a depth of 361 m underground in bedded salt on December 10, 1961. The test site for Project Gnome was located about 48 km southeast of Carlsbad, New Mexico.

The Gnome experiment was conducted in the Salado rock formation of Permian age (Fig. 1.1). This formation in the vicinity of the explosion is composed of about 89% halite, or rock salt (NaCl), 7% polyhalite [$\text{Ca}_2\text{MgK}_2(\text{SO}_4)_4 \cdot 2\text{H}_2\text{O}$], 1% anhydrite (CaSO_4), and 3% silt and clay. The impurities occur primarily as separate beds interlayered with the salt strata, although they also occur mixed with the salt crystals (Appendix A and B). Overlying the Salado formation are the sedimentary limestones, dolomites, sandstones, claystones, and siltstones of the Rustler and Dewey Lake Formations of Permian age and alluvial deposits of Quaternary age (Reference 1).

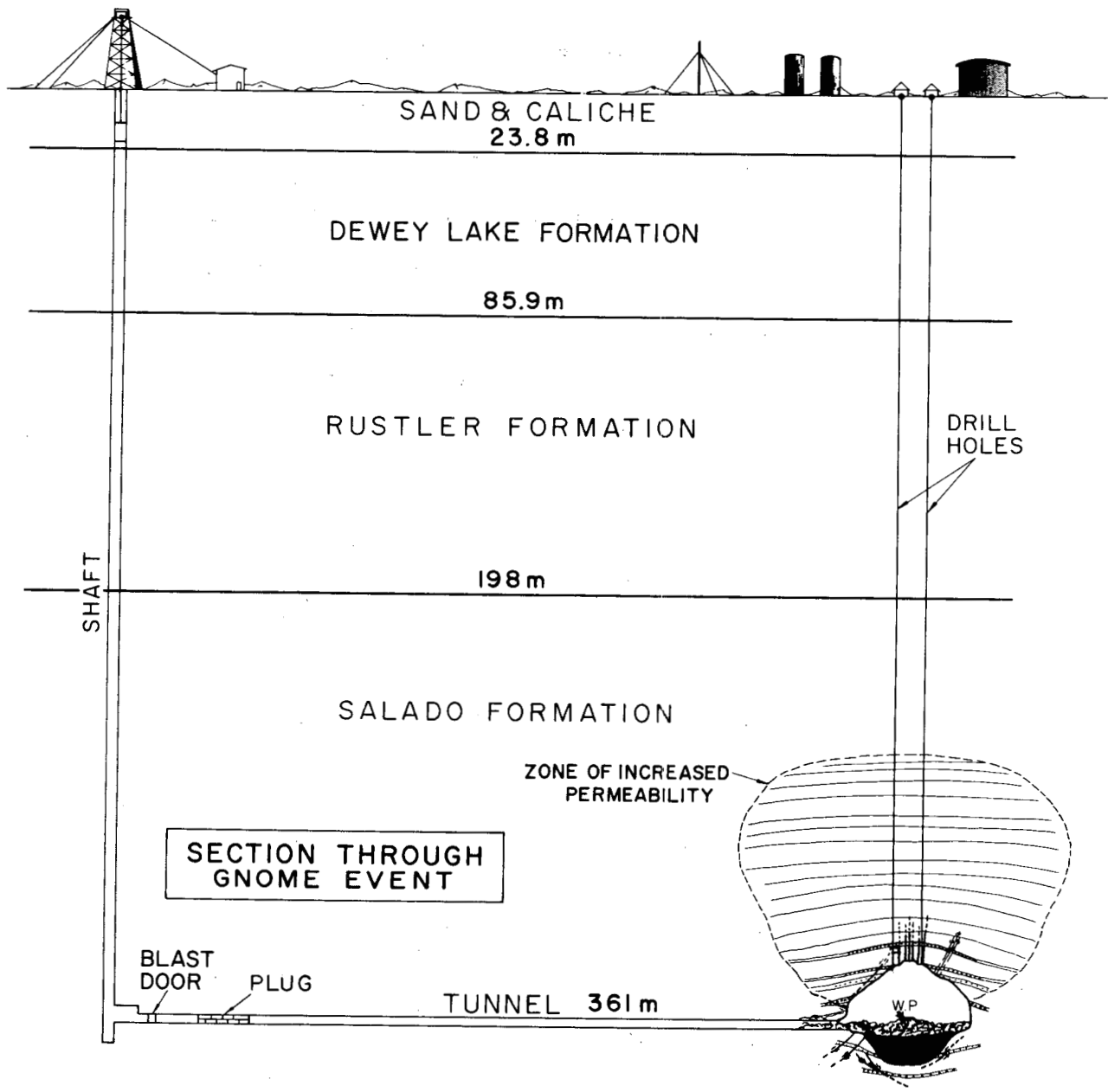


Fig. 1.1 Vertical section through the Gnome postshot environment.

The Gnome device was emplaced at the end of a buttonhook-shaped drift, a distance of 301 m from the shaft (Fig. 1.2). The first 274 m of the drift were straight along a line between the shaft and the device. The remainder was curved and is referred to as the "buttonhook" portion. The drift was designed so that the buttonhook would close following the detonation and contain the explosion. Requirements for an associated neutron-physics experiment were such that most of the drift had to be line-of-sight to the device. An evacuated pipe (the "neutron pipe") extended from a revolving wheel (the "neutron wheel") through the straight portion of the drift and continued through a drill hole to the device room. Backup stemming was provided in the drift near the shaft to restrict venting if the close-in stemming failed.

1.2 OBJECTIVES

The major objective of the postshot exploration program was to provide a definition of the environment created by the detonation in support of the primary object of Project Gnome: To study the effects of an underground nuclear explosion in salt. Previous experience with volcanic tuff and alluvium at the Nevada Test Site had provided a general understanding of the interaction between nuclear explosions and rock materials. An explosion in salt provided an excellent test of this understanding, since the physical and chemical properties of salt are greatly different from those of tuff and alluvium.

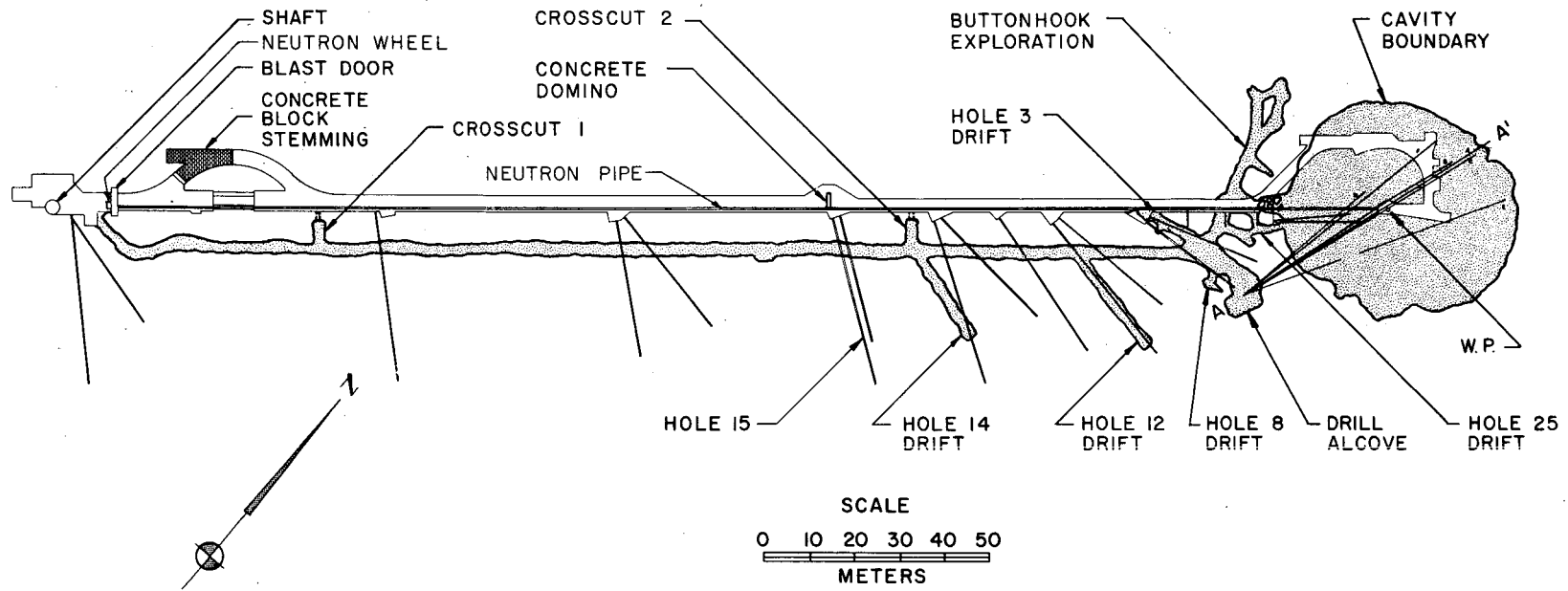


Fig. 1.2 Plan view showing the post-explosion exploration and cavity (shaded) (the fine line drawing indicates the pre-detonation configuration).

Many data were also obtained pertaining to some of the other objectives of the experiment, specifically:

1.2.1 The Isotopes Program: To determine the feasibility of recovering radioisotopes produced by a nuclear explosion. This method would represent a significant alternative to reactor methods. Although the device used in Gnome was not specifically designed to produce quantities of useful isotopes, the mixed fission products made possible a feasibility study.

1.2.2 The Power Program: To investigate the feasibility of the measurement and extraction of heat deposited by the explosion. It had been suggested that the heat of fusion of the salt melted by the explosion might be extracted and used for electrical power.

1.2.3 Shock Effects Studies: To subject a variety of mineral and organic samples to a range of shock pressures produced by the explosion in order to determine the effects of the explosion (in terms of phase transitions, property changes, etc.) on the samples.

The purpose of re-entry drilling from the surface was to provide radioactive samples for yield determination; to enable measurements concerned with the power feasibility studies; and to provide preliminary definition of the environment created.

1.3 EXPLORATION PHASES

Post-detonation exploration consisted of: 1) examination of the surface facilities and the ground surface over the working point* (Reference 2); 2) examination of the shaft and the bottom station six days following the detonation (Reference 2); 3) re-entry drilling from the surface into the cavity region during the period from December 11, 1961 to January 18, 1962; 4) underground mining and drilling exploration, including re-entry into the emplacement drift, recovery of shocked samples and instruments, entry into the cavity produced by the explosion and general definition, by direct observation, of the postshot environment. Exploration was complete by the end of September, 1963. This report covers the work accomplished during phases 3 and 4.

1.4 OBSERVATIONS IMMEDIATELY FOLLOWING THE EXPLOSION

Less than one minute following the explosion, radiation was detected at the blast door near the bottom of the shaft (Fig. 1.2) by remote-area radiation monitors. No radiation was detected at the shaft collar until three minutes and forty seconds after the detonation. At approximately seven minutes after zero time, a gray smoke, steam, and associated radioactivity surged from the shaft opening. By eleven minutes following the explosion, copious quantities of steam issued from both shaft and ventilation lines. A large flow continued for

*The location of the nuclear device.

about thirty minutes before gradually decreasing. A small flow was still detected through the following day. The radioactive elements that vented through the shaft were volatile and noble gases (Reference 3).

The unexpected venting of steam and associated radioactive gases led to an additional objective for the exploration program - the determination of the cause and nature of venting.

The Gnome event was monitored by geophone arrays from shot time until the shot environment was penetrated by re-entry drilling. The geophone records indicated that noise produced by rock movement lasted for three minutes following the explosion and were very infrequent after that time.

CHAPTER 2

THE CAVITY ENVIRONMENT

2.1 GENERAL

Postshot exploration started first from the surface and then was accomplished by drilling and drift excavation underground (see Fig. 2.1).

On May 17, 1962, only five months after the explosion, excavation along preshot drill hole #25 for the purpose of recovering shocked samples resulted in actual personnel entry into the cavity. This made possible direct observation of the cavity interior, photographic documentation and a minimal triangulation survey to define its size and shape (Fig. 2.1). At that time, the air temperature was 50°C near the cavity entrance, the relative humidity was 60-70%, and the radiation levels varied from place-to-place, but were rarely in excess of 20 mR/hr. One month later a more comprehensive temperature survey indicated a variation between 50 and 57°C within the cavity. It should be noted that for several weeks prior to and following cavity entry, fans located in drill holes from the surface into the cavity had flushed several million cubic meters of air through this environment.

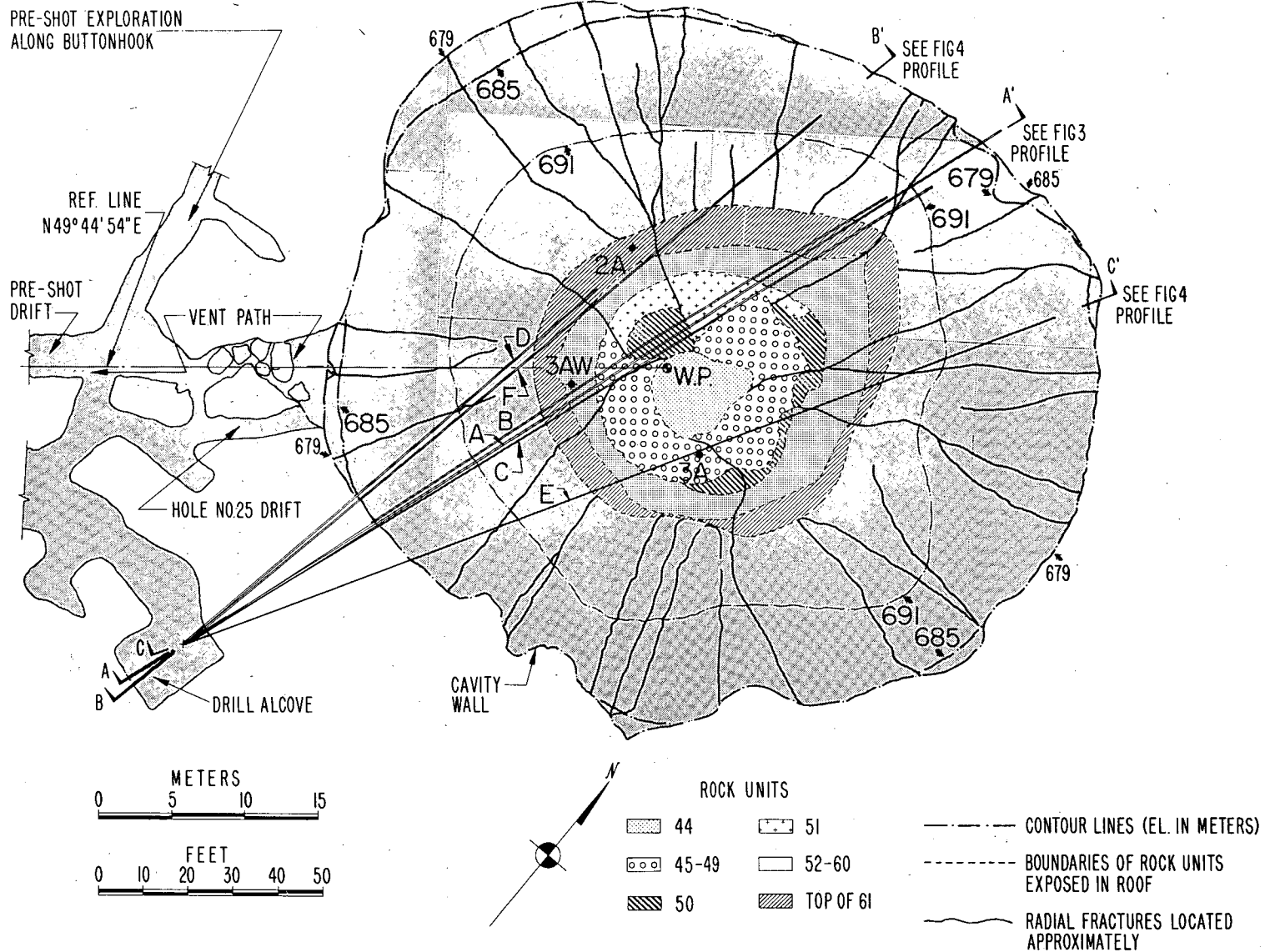


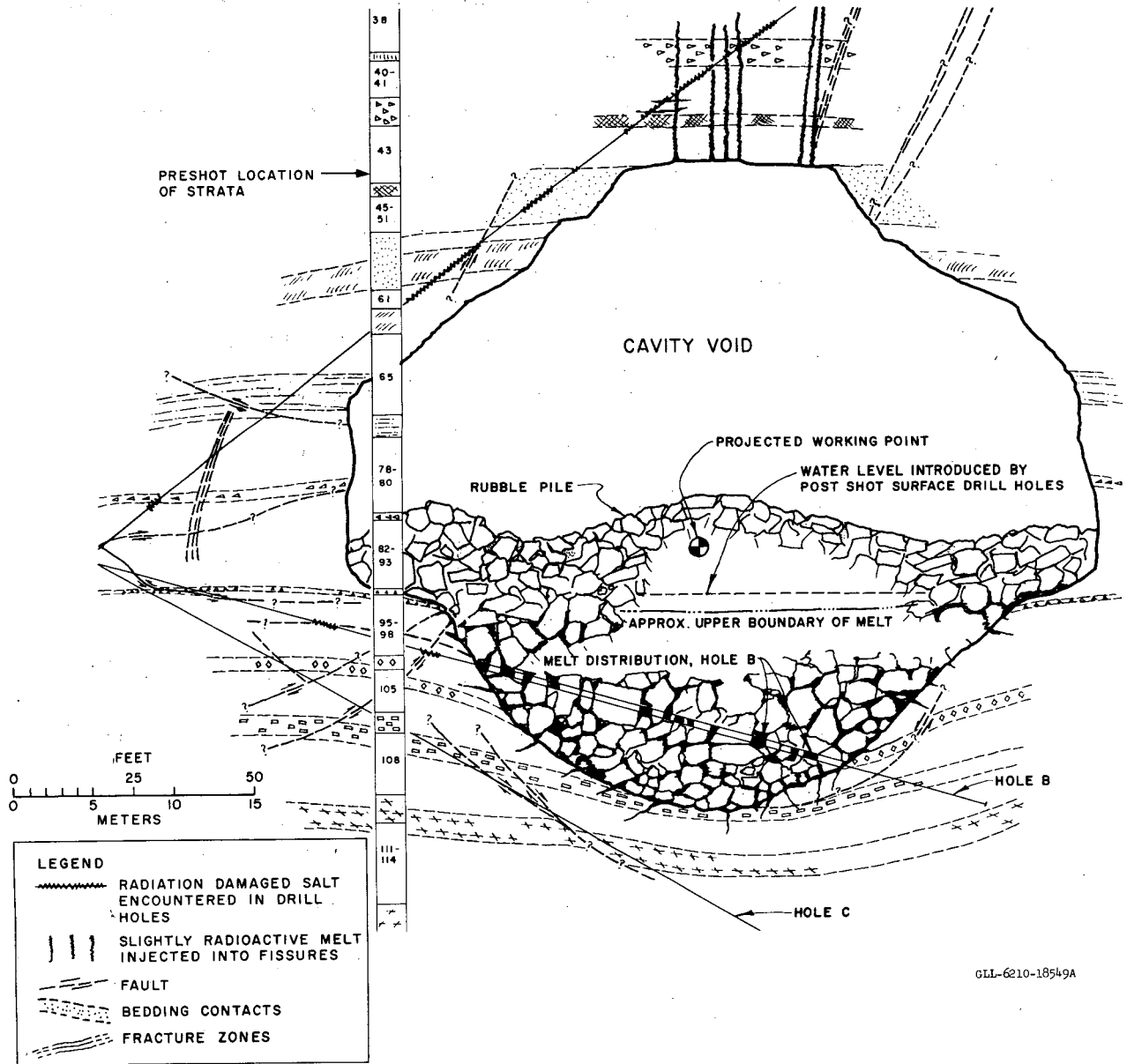
Fig. 2.1 Gnome cavity: reflected ceiling plan.

2.2 CAVITY VOLUME AND SHAPE

An estimate of the total void volume produced by the explosion was made, using a combination of three points from drill holes penetrating the top of the cavity, photographic guides for extrapolation from survey control within the cavity, and underground drill holes which defined the cavity below the working point in 10 places. This volume was calculated to be 27,200 cubic meters (Appendix D) and is in very good agreement with a measurement made by pressurizing the cavity with compressed air. A known volume of air at a known pressure was introduced into the cavity. From these measurements the cavity volume was calculated to be $28,000 \pm 2,800$ cubic meters (J. Tracy, LRL - verbal communication).

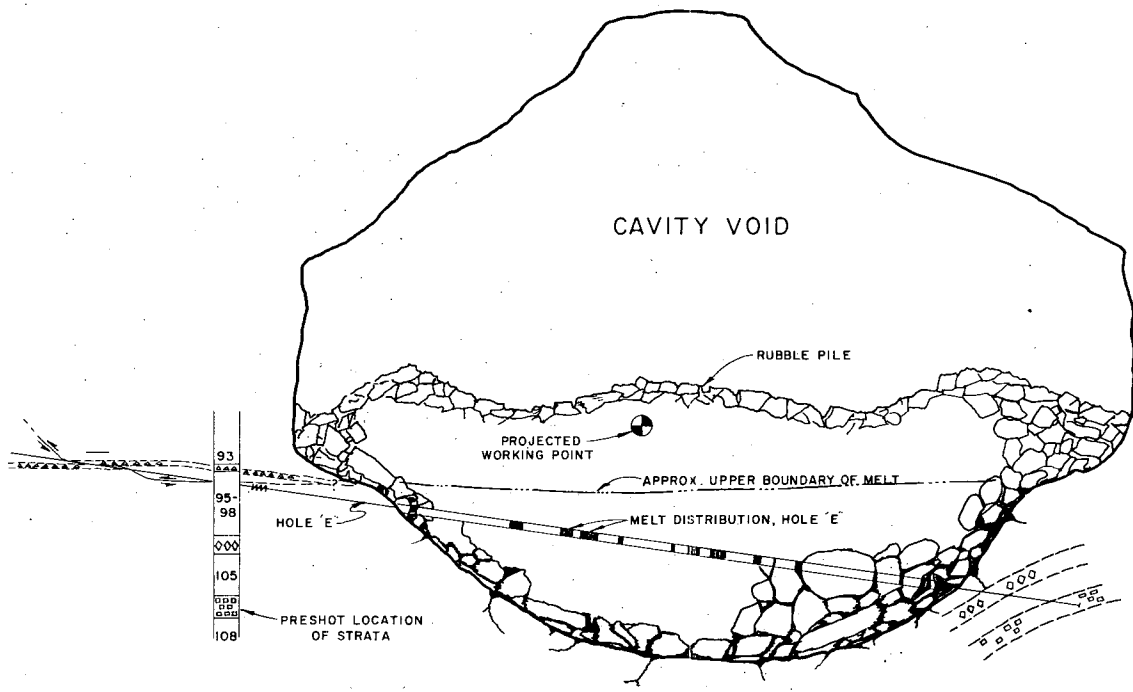
The total void volume of 27,200 cubic meters is equivalent to a sphere with a radius of 18.7 meters. The cavity is asymmetric, however, because of anisotropic resistance to cavity expansion, implosion of the cavity walls, and partial ceiling collapse (see discussion in Chapter 3). The cavity shown in Figs. 2.2 and 2.3 has an average radius of 17.4 m in the lower portion (measured from the working point to the boundary of radioactive melt); an average radius of 24.4 m in the equatorial plane; and an average radius of 22.9 m in the upper portion (measured from the working point to the rock-void interface). The shape of the ceiling of the cavity indicates that the major pre-shot weaknesses in the rock, the bedding planes or horizontal boundaries between

GNOME CAVITY CROSS SECTION 3 kt

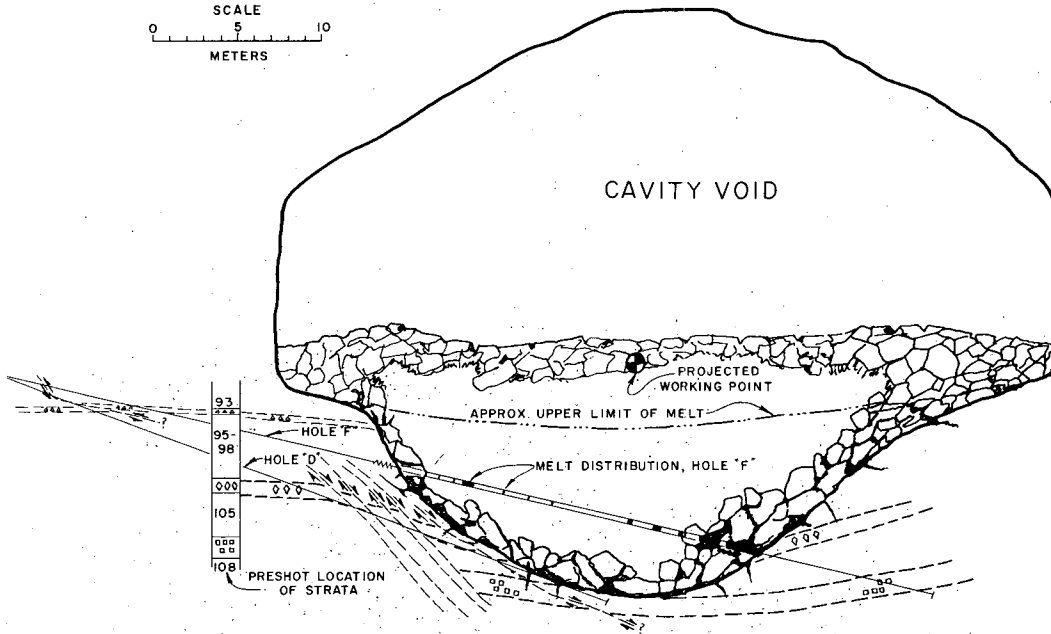
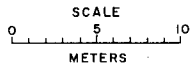


GLL-6210-18549A

Fig. 2.2 Cavity profile A-A' (see Fig. 2.1 for plan view).



CAVITY PROFILE C-C'



CAVITY PROFILE B-B'

Fig. 2.3 Cavity profiles B-B' and C-C' (see Fig. 2.1 for plan view).

rock units, somewhat controlled the extent of collapse. It is very likely that less collapse would have occurred if these weaknesses had not existed.

The most significant departure from spherical symmetry is a girdle of rock about 9 m high surrounding the equatorial region of the cavity. This region moved radially further from the working point than rock nearer the base or top of the cavity. The development of this asymmetry was most likely controlled by bedding plane weaknesses and thin horizontal clay strata that separated more competent beds of salt and polyhalite. The explanation of this bulge is discussed further in the sections on permanent displacements and earth deformation. The cavity would be more symmetrical about a vertical axis passing through a point about 4 m northeast of the working point rather than through the working point (the center of the nuclear device). This displacement of the effective center of energy may be due to the shape of the chamber in which the device was detonated, resulting in the initial distribution of the explosion energy as a cylindrical source rather than a spherical one.

2.3 RUBBLE AND ASSOCIATED RADIOACTIVE MELT

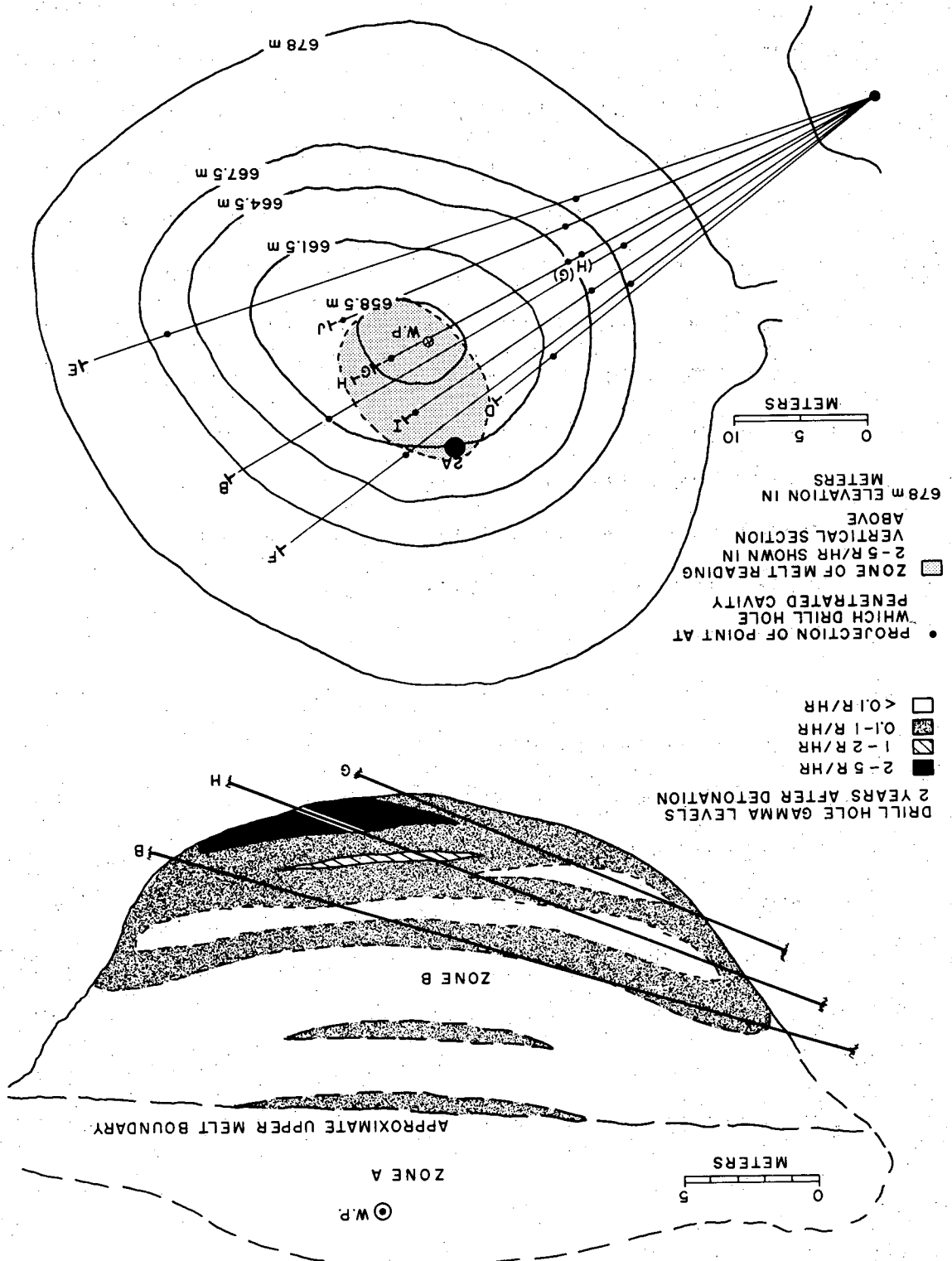
The mass of rock melted by the explosion, based on the analysis of ore recovered from drill holes, is estimated to be about 3.2×10^6 kg, equivalent to about 10^6 kg per kiloton of yield.

This mass compares favorably with the expected mass vaporized and melted of about 1.4×10^6 kg per kiloton. This prediction was based on the assumption that 41% of the explosive energy is utilized in melting the rock (Reference 4). The melt became intimately mixed with about 11.6×10^6 kg of rock, much of which was probably imploded, decrepitated, or fell into the cavity early during the first few seconds following the explosion. An estimated 13.6×10^6 kg of rock collapsed later from the upper hemisphere and blanketed the region containing the radioactive melt breccia at the cavity base (Appendix D).

The region denoted as Zone B in Fig. 2.4 can generally be described as a rock-melt breccia in which the melt forms much of the matrix between the larger rock fragments (the range of particle diameters is estimated to be about 15 cm to 3m). The melt itself engulfs smaller rock fragments that range in diameter from a fraction of a centimeter to a few centimeters. The degree of dilution of samples of the melt varies greatly from almost no rock fragments to as much as 30 or 40 percent.

Because much of this zone is typically a mixture of rock fragments cemented together by the melt matrix, it is likely that this material would be self-supporting if actual mining re-entry were necessary. This is especially true near the cavity boundary where the concentration of melt is the highest. Most likely, a liberal amount of rock support would be necessary.

Fig. 2.4 Schematic sections through the Gnome cavity showing approximate distribution of radioactivity two years after the explosion.



This material was sufficiently self-supporting, however, that the drill holes remained open without casing.

The rubble in Zone A, Fig. 2.4, above the zone containing radioactive melt is essentially a loose pile of rock fragments and is not self-supporting. During re-entry drilling the holes caved in this region, causing considerable difficulty. In this zone, the particle-size variation can be approximated with reasonable accuracy by direct observation of the rubble surface exposed at the base of the cavity void. The range in particle size is extremely large, varying from crushed rock fragments less than 1 cm across to large blocks as large as 7 m across the maximum dimension. Blocks exceeding 2 m across account for less than 10 percent of the rubble and the average particle diameter is about 75 cm.

The explosion liberated at least 5×10^4 kg of water from the vaporized and melted rock and an additional 17×10^4 kg or water could have been liberated from the 11.6×10^6 kg of rock that came from the cavity wall and was mixed with the melt. M. Nathans (Reference 5) calculated from the tritium concentration in the vented steam that as much as 4×10^5 kg of water might have been liberated from the rock. Had there not been venting to tap off much of this water, it would have eventually condensed and collected in the voids of the rubble at the base of the cavity. As it was, the water level in the rubble was at an elevation of 673 m, or 2.1 m below the working point. Most of

this water was added during surface re-entry drilling, although some is probably condensed steam that did not escape during cavity venting. A total of about 5×10^5 kg of water entered the cavity and the voids in the rock above the working point as a result of circulation losses during drilling. Water was still dripping very slowly into the cavity one year following the explosion.

As discussed above, the radioactive melt forms a puddle intimately mixed with nonradioactive rock. A schematic cross section through the lower hemisphere of the cavity (Fig. 2.4) shows the approximate gamma radiation distribution based on radiation log data from underground drill holes and hole 2a. This picture is largely conceptual, since it is based on limited data and the logs show a great deal of scatter in radiation levels because of the large amount of nonradioactive rock mixed with the radioactive melt.

This figure shows a zone at the base of the cavity that is highly enriched in radioactivity. In vertical hole 2a a 0.6-m-thick zone had radiation six times levels greater than any other level recorded in this hole. Underground holes, G through J, were drilled in August, 1963, to better define this zone and to obtain additional radioactive samples for the isotopes production study. Data from these holes were used primarily to define the limits of the enriched zone indicated in Fig. 2.4.

Presently the rubble and melt are being studied in detail in order to determine methods of processing this "ore" for elements that are chemically similar to the actinides. A report by M. Nathans (Reference 5) covers the details of this study. It has been determined that almost all of the fission products (other than the gaseous or volatile ones) remain with the salt impurities when samples are either dissolved in water or remelted to separate the NaCl from the other impurities. Part of the scope of this study is to determine with which chemical species the different radio-elements are associated.

It is interesting to note that the mineral olivine, specifically forsterite (Mg_2SiO_4), makes up a significant portion of the water-insoluble fraction of several samples. This mineral did not occur preshot in the rock. The major source of magnesium was the mineral polyhalite [$\text{Ca}_2\text{MgK}_2(\text{SO}_4)_4 \cdot 2\text{H}_2\text{O}$]. Magnesium also occurs in the clay minerals and in trace quantities of magnesite (MgCO_3). Silica occurs primarily as silt-sized quartz particles and with the clay minerals. Reference 5 also describes a variety of other chemical reactions resulting in several compounds and the radioactivity fractionation associated with these species.

Examples of the solidified salt melt are shown in Fig. 2.5. Sample B-21H is only slightly vesiculated. It was taken from about 2 m from the far cavity boundary in drill hole B (Fig. 2.2), and contains a large amount of rock fragments, presumably blown

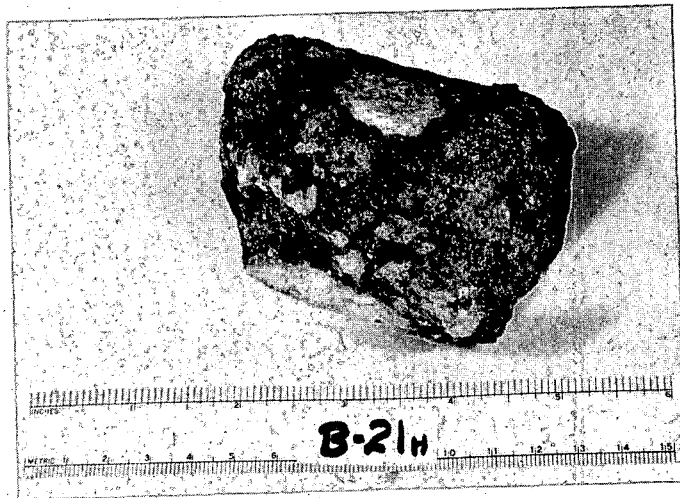


Fig. 2.5 Typical melt samples from underground drill holes.

off the cavity walls. Some of the fragments underwent fusion because of the superheat of the melt. Sample F-21H is from drill hole F (Fig. 2.3) near the cavity edge. The melt in contact with the unfused salt forms a dense band in contrast with the vesicular melt on the other side of the band. It is interpreted that following cavity growth the rock bounding the cavity broke up and imploded, allowing the salt melt to invade openings that resulted. The newly exposed colder rock quenched the melt, forming unvesiculated melt at the contact. Under normal circumstances, it would be expected that this chilled border would be gradational, but at Gnome it is quite possible that when venting occurred, the cavity pressure dropped rather abruptly, causing violent out-gassing of the melt. This sudden out-gassing, which was closely followed by solidification of the melt, produced vesiculation. Sample E-3H was taken from drill hole E near the central portion of the cavity about 25 ft above the cavity bottom (Fig. 2.3). This melt cooled more slowly than most of the melt observed and developed large crystallites - up to 4 mm in diameter. Most of the melt solidified rapidly and is fine-grained - less than 1 mm.

2.4 ROCK TEMPERATURES

A plot of temperature versus radial distance from the working point is shown in Fig. 2.6. Data points shown were taken from

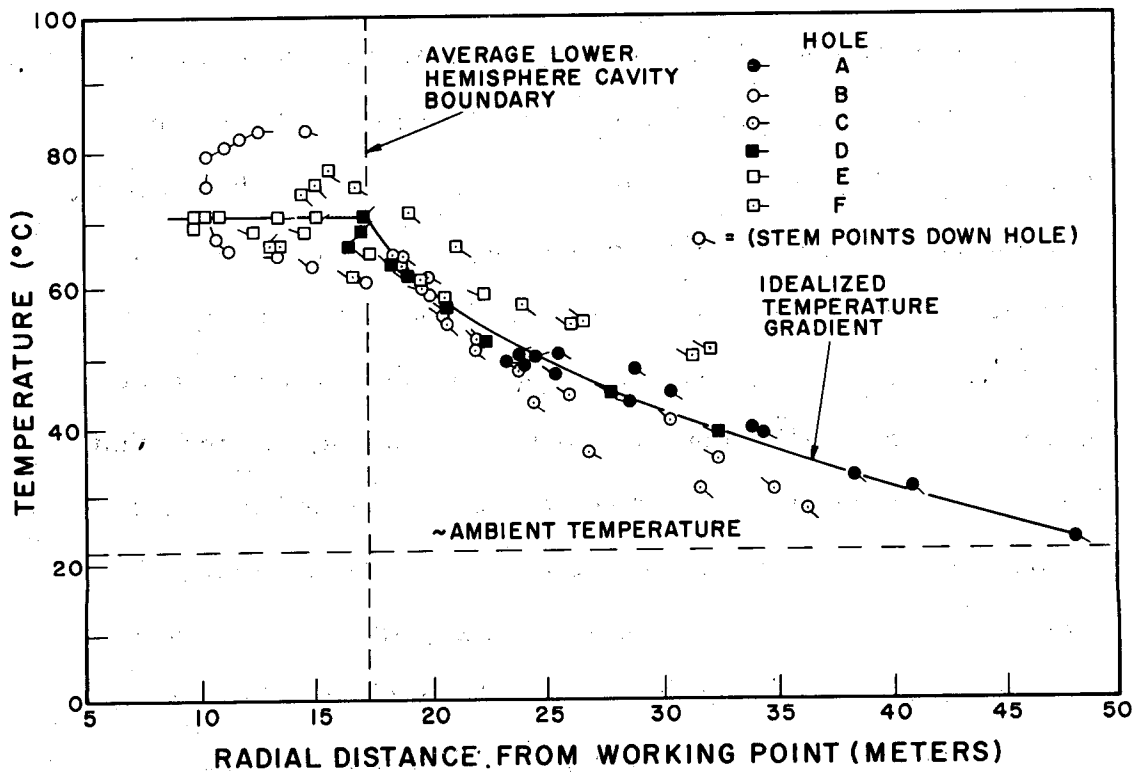


Fig. 2.6 Temperature vs radial distance from working point six months after the detonation.

temperature measurements made about 6 months after detonation, in drill holes A through F. This plot indicates that the average temperature was 71°C in the rubble-melt zone of the cavity at that time. Temperatures varied from 63 to 83°C in this region, depending upon the elevation at which the measurement was made. Maximum temperatures were recorded within about 1 m from the lower cavity boundary in each hole that penetrated this zone.

The logs of holes B and C indicate that below the cavity, at equal radial distances from the working point, and at equal angles from the vertical; temperatures are 10-12° higher in a northerly

direction than in the southerly. This asymmetry is consistent with the asymmetrical position of the zone of highly-radioactive melt described previously.

CHAPTER 3

PERMANENT DISPLACEMENTS

3.1 GENERAL

Displacement of the material surrounding the Gnome explosion has been measured laterally at a distance of 298 m by gages in a drill hole (Reference 6), and the permanent displacement of the surface over the working point is known by surveys (Reference 7). In addition, permanent radial displacements have been determined from preshot and postshot positions of rock strata and other markers such as instrument holes.

Preshot elevations of beds were obtained from the USGS lithologic log (Reference 8) and tunnel map (Reference 1). Postshot positions were determined from geophysical logs of the vertical holes and from core from the underground inclined drill holes. Preshot and postshot positions of beds are generally known within ± 0.3 m. The locations of instrument holes branching off from the main drift were accurately surveyed before and after the detonation.

Figure 3.1 is a plot of the permanent displacement data obtained by postshot underground exploration. R_i - the preshot radial distance of a given point from the working point - is plotted against $1/(R_f - R_i)^2$, where R_f is the corresponding postshot radial distance from the working point. For convenience, a scale showing values for $(R_f - R_i)$ is on the plot and a theoretical curve drawn based on the relationship

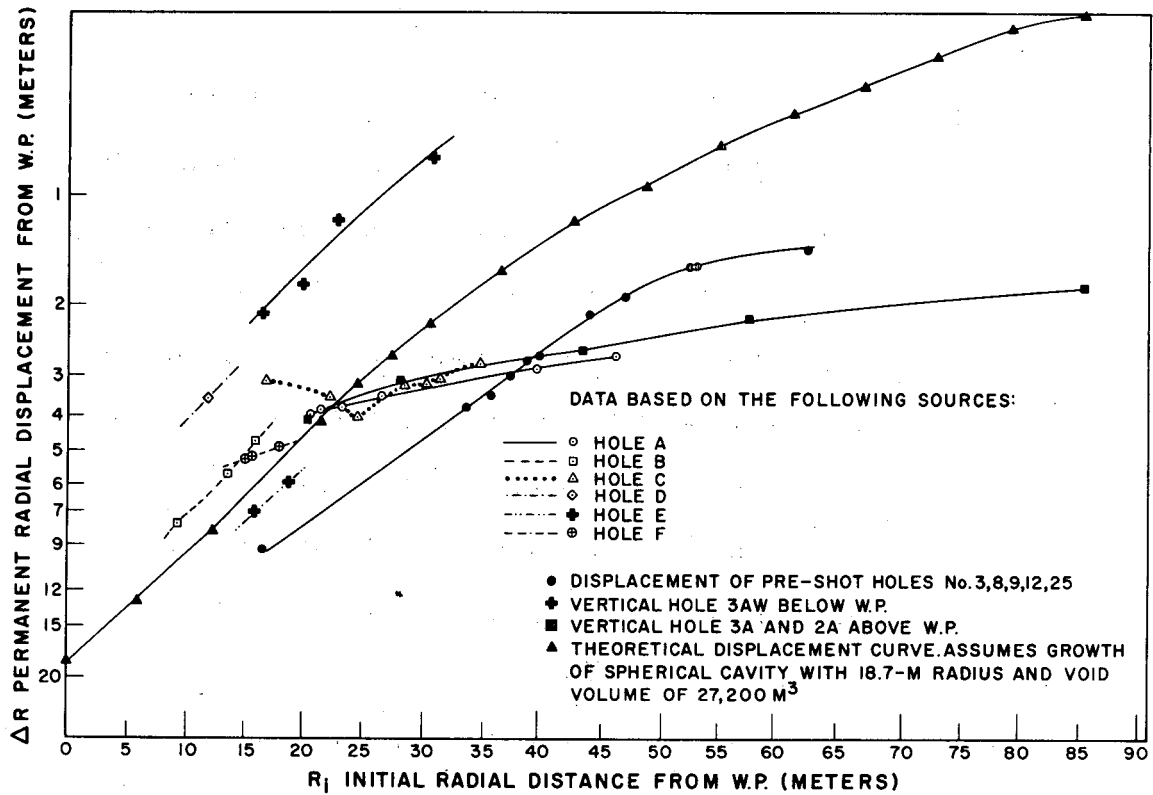


Fig. 3.1 Permanent rock displacement vs distance from working point.

$R_c = [R_f^3 - R_i^3]^{1/3}$ (Appendix C). In this equation, R_c is a theoretical radius of the void produced by the explosion. Assuming a void volume of 27,200 m³ resulting from the growth of a spherical cavity, R_c is equal to 18.7 m. The systematic departures of the data from the theoretical curve are discussed below.

3.2 DISPLACEMENTS SURROUNDING THE CAVITY

Permanent displacements of rock strata were obtained from the records of holes drilled below the working point (drill holes B, C, D, E, F, and 3AW). These displacements generally plot above the theoretical curve for given R_i values, indicating R_c is less than

18.7 m in this region. The average value for R_c calculated from these data is 16.3 m. Permanent radial displacements of instrument holes #3, 8, 9, 12, and 25 fall below the theoretical curve, thus indicating that R_c in the equatorial region is greater than 18.7 m. The average value for R_c calculated from these data is 22.9 m. The displacement at 298 m was about 3.5 cm at 0.5 sec after the explosion, measured by gages in a drill hole at the elevation of the working point (Reference 6). The R_c of 21 m calculated from this displacement compares favorably with the average R_c calculated from instrument-hole data.

Permanent-displacement data in the equatorial region and below the working point generally have nearly constant R_c values, and the slopes of these curves usually parallel the theoretical curve (Fig. 3.1). Variations of R_c can generally be explained by differential motions of rock along fault planes revealed in the mining and drilling exploration.

Applying the theoretical equation to the displacement data obtained above the working point (drill holes A, 2A, and 3A), it is found that R_c increases with radial distance from the working point and the slopes of the curves do not parallel the theoretical curve, but are less steeply inclined.

These data indicate an asymmetrical distribution of rock displacement surrounding the cavity, implying different phenomena above the cavity relative to the equatorial region and below the cavity. This is further discussed in Section 3.3.

3.3 IMPLICATIONS OF LOCALIZED UPLIFT BETWEEN THE CAVITY AND THE GROUND SURFACE

The asymmetry of the rock displacement associated with cavity growth and subsequent rock motions may be explained in the following manner:

A reasonable assumption is that the force resisting cavity growth is about equal to the weight of the overlying rock. In Gnome, the observed asymmetry in the equatorial region indicates that this force was nonuniformly distributed. The growing cavity met less resistance horizontally, in the direction of the inherent weakness in the rock; i. e., bedding planes between various rock strata. Thin clay seams between halite and polyhalite strata are most conspicuous in that they form both structurally weak planes and lubricated glide surfaces.

Immediately following an underground nuclear explosion, a shock wave is produced by the impact of the expanding hot gases with the confining rock medium. This shock wave travels to the surface, where it is reflected back toward the cavity region. As the rarefaction wave returns from the surface, the upper several hundred feet of rock is spalled (goes into free fall) which also momentarily decreases the overburden pressure. At that time the compressed rock can adjust and much of the cavity volume is transferred from compressed rock into upward unloading and permanent surface doming. Local cavity growth can also occur, since the gas

pressure within it may well exceed the overburden pressure while the upper few hundred feet of rock is spalling.

From the elevation about 105 m above the working point down to the cavity, the rock was found to be significantly more porous and permeable than it was preshot. This phenomenon resulted in circulation losses while drilling from the surface and was observed by comparing preshot and postshot sonic geophysical logs. The permeability is primarily associated with bedding plane partings and extends at least 46 m laterally from the working point as evidenced by circulation losses in USGS drill hole #6 (Reference 9). At the far end of drill hole A, Fig. 2.1, faulting above the cavity was encountered in which the rock over the working point was dropped downward relative to the rock lateral to the working point. These data suggest that there was an inward sag or down-drop towards the cavity of rock strata above the working point. The backdropping of strata occurred for a distance of about 105 m vertically above the working point. This movement is superimposed upon a general uplift of the rock between the cavity and the surface. Both of these motions are in addition to the rock motion associated with cavity growth that took place primarily during the first 75 to 100 msec following the explosion.

Near the top of this permeable zone, at 85 m above the working point, where backdropping of strata is minimal, the difference between the ΔR (i. e., $R_f - R_i$) on the theoretical curve (Fig. 3.1)

and the ΔR shown on the curve from drill hole 2A and 3A data, is almost 2 m. From the existing data, a minimum of 2m is the best estimate of the magnitude of the uplift of the rock up to 85 m above the cavity that is additional to the upward deformation associated with cavity growth during the first 100 msec.

Uplift is probably a little greater in the rock immediately above the cavity since gross permeability and associated porosity increases were observed as high as 105 m above the working point. This amount of uplift assumes a maximum initial cavity radius R_c of 18.7 m prior to uplift (see Section 3.4).

Doming at the surface was spread over an area about 360 m in radius (Reference 2), and had a maximum permanent vertical displacement of 0.6 m. The uplift of rock near the ceiling of the cavity represents only a small volume increase relative to the total cavity volume or the volume represented by permanent surface uplift. Further evidence supporting the hypothesis that an uplifted plug is formed is given in Section 4.1.

The cone-shaped uplifted zone shown in Fig. 3.2 indicates that a possible effect of backdropping of some of the rock is to tighten up the arch over the cavity, rather than weaken it. This process may have been important in producing cavity stability. The lack of a significant number of open fractures above the cavity to interconnect the preshot structural weaknesses in the rock is very important from a radiation-safety point of view. The radial

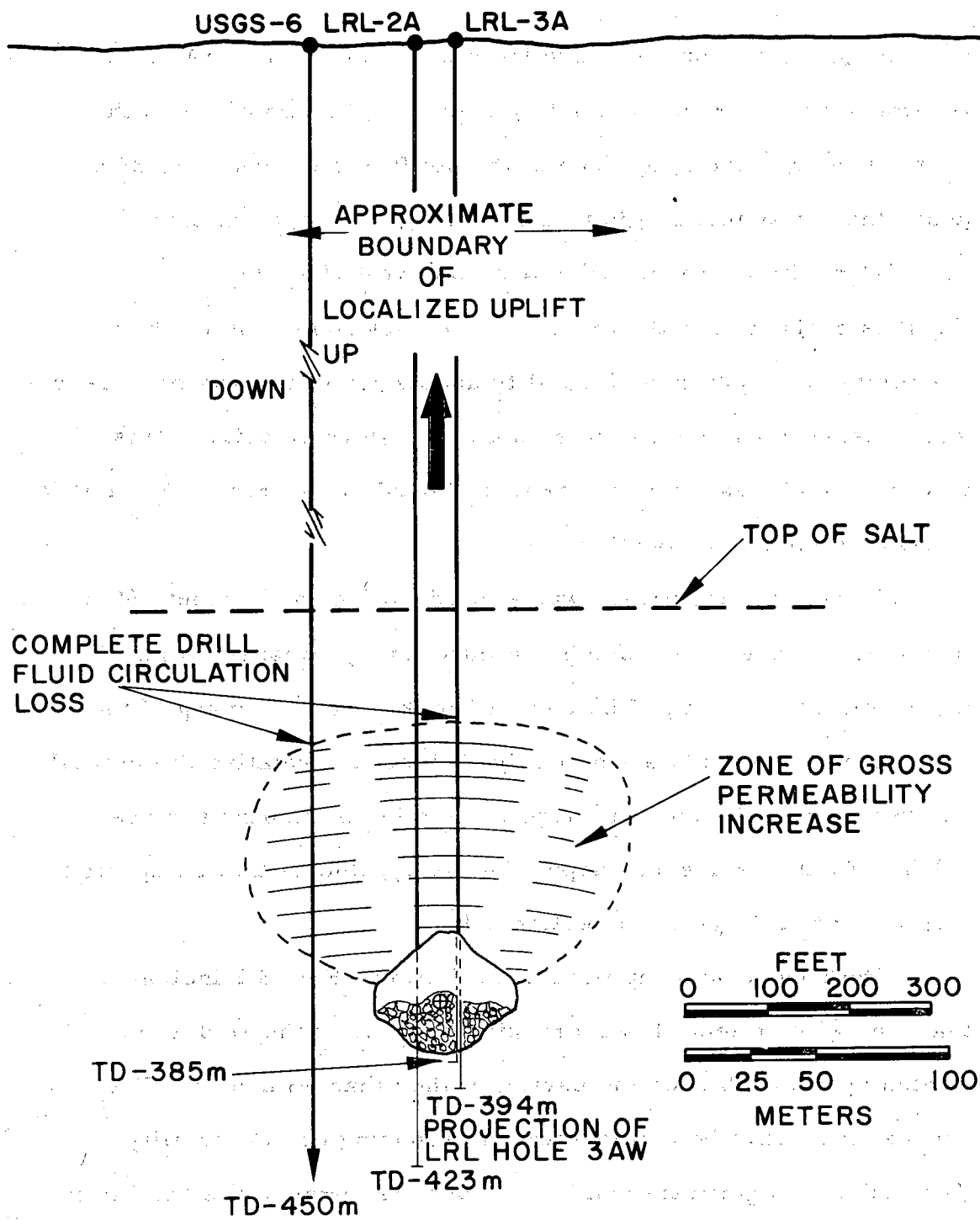


Fig. 3.2 Vertical section showing configuration of localized uplift.

fractures that were produced by the explosion were filled with melt, sealing in the gases.

3.4 SUMMARY OF CAVITY RADII AND IMPLICATIONS ABOUT "BLOW-OFF" OF THE CAVITY WALLS

As pointed out in Section 3.1, R_c is the radius of the theoretical cavity void. The void produced by the explosion is equivalent to an 18.7-m-radius sphere; and the average value of R_c below the working point is 16.2 m, contrasted to an average of 22.9 m in the equatorial region of the cavity. R_c above the working point cannot be greater than about 18.7 m and be consistent with the measured cavity volume. Table 3.1 summarizes values of R_c , and compares these with the final cavity radii defined on p. 17.

TABLE 3.1 THEORETICAL AND FINAL CAVITY RADII COMPARISON

	R_c , Radius of Theoretical Cavity Void (m)		Final Cavity Radius (m)	
	Range	Average	Range	Average
Below the working point	12.5-21.9 ^a	16.2	14.9-19.8 ^c	17.4
Equatorial region	21.0-26.2 ^b	22.9	19.5-30.2 ^d	24.4
Above the working point	Maximum of	18.7	20.4-27.1 ^e	22.9

^a 20 data points

^b 11 data points

^c 10 data points

^d 25 data points

^e 15 data points

Much of the variation in both R_c and final cavity radii shown by the range values in the table can be explained by observed differential movement of rock along fault planes discussed in Section 4.3 on rock deformation.

In the region below the working point and in the equatorial region, the difference between the average radius of the cavity void (R_c) and the final cavity radii is about 1.2 m. It seems probable that this thickness represents an annular shell of the cavity wall that breaks up, decrepitates, spalls, or is imploded into the cavity. Thus openings develop in the rock bounding the lower hemisphere of the cavity and the fluid, radioactive salt melt invades these openings. The extent of the melt defines the final cavity boundary. This annular zone is called the "blow-off" zone; it produces the rock that blows into the cavity where it mixes with and cools the melt. Assuming that the average thickness of this zone is 1.2 m surrounding an 18.7-m-radius sphere, then about $5.6 \times 10^3 \text{ m}^3$ of rock mixed with about $3.2 \times 10^6 \text{ kg}$ of melt in the rubble is "blow-off" material from the cavity walls. The difference between $5.6 \times 10^3 \text{ m}^3$ and the estimated total rubble volume is $11.46 \times 10^3 \text{ m}^3$, which would roughly, be the amount added by ceiling collapse into the cavity. Figure 6.1b is a schematic drawing illustrating the "blow-off" phenomena and the various dimensions discussed above. Appendix E is a further discussion of the rubble distribution.

CHAPTER 4

FRACTURING AND DIFFERENTIAL ROCK MOTIONS

4.1 LOCAL UPLIFT OF STRATA OVER THE SHOT POINT

The existence of an uplifted region over the shot point was inferred on the basis of permanent displacement data and a mechanism for its formation was discussed in Section 3.3. Additional evidence pointing to its existence and crudely defining its shape is discussed in this section. Figure 4.1 is a map of the ground-surface

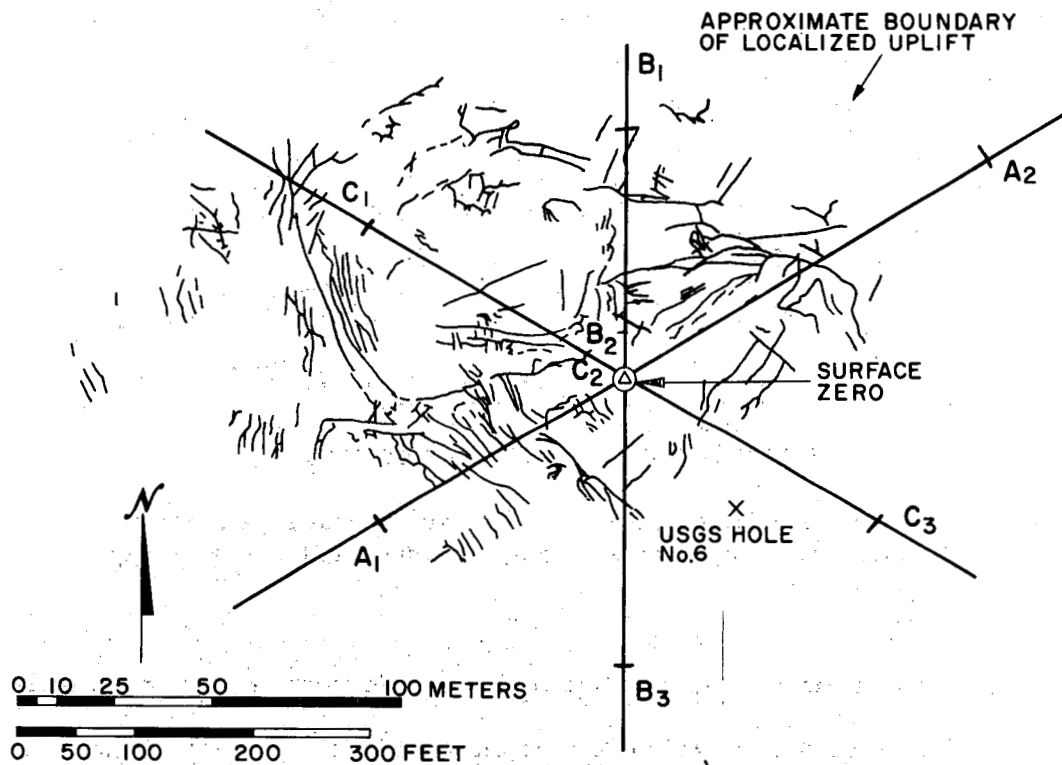


Fig. 4.1 Map of Gnome ground surface showing fractures and approximate boundary of uplifted region (modified after Fig. 4.2 of Reference 2).

fracture pattern produced by the explosion as mapped by Hoy and Foose (Reference 2). Figure 4.2 shows permanent-displacement profiles of the ground surface along Section A_1-A_2 , B_1-B_3 , and C_1-C_3 located in Fig. 4.1. As these profiles show, the surface

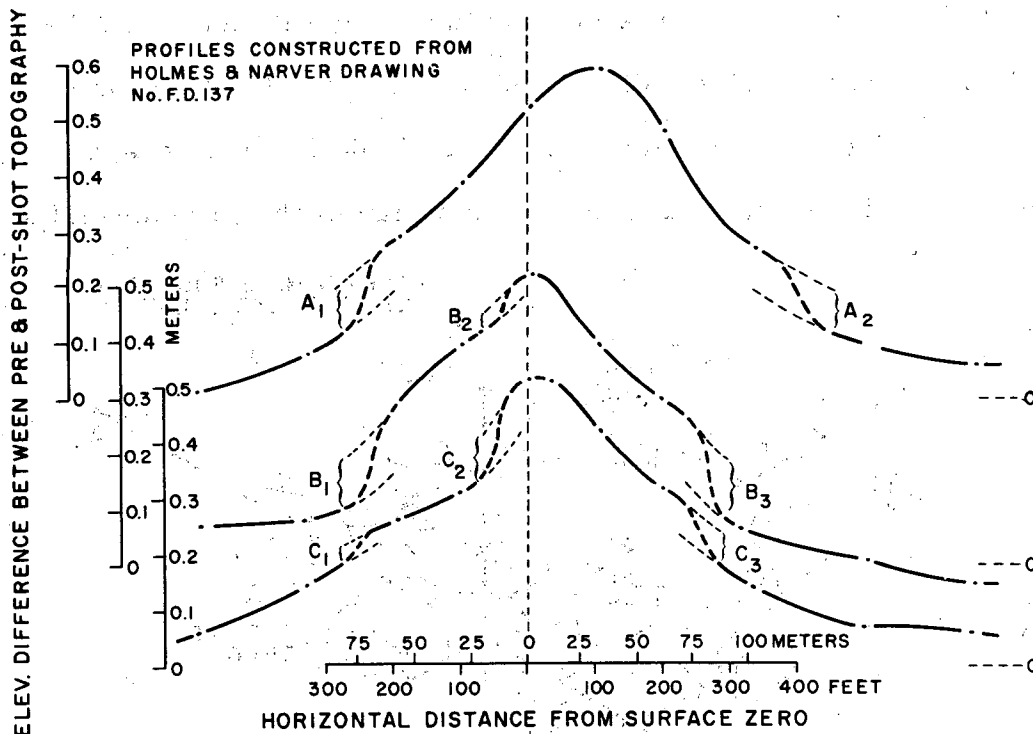


Fig. 4.2. Profiles of the Gnome ground-surface permanent displacements showing the uplifted region configuration (see Fig. 4.1 for plan view).

doming is not a smooth arch, but there are locations of abnormally large uplift or differential rock motion within fairly restricted zones (A_1 , B_1 , A_2 , B_2 , etc.). It is suggested that these zones may be the locations of the boundary of the uplifted region. Figure 4.1 shows the trace of these boundary zones based on the survey data and there

is a parallelism between this trace and the trace of observed surface fractures.

The USGS drilled vertical hole #6 at a distance of 46 m from surface ground zero. This hole encountered fractures at depths of 122 and 183 m from the surface (Reference 9). This fracturing may be associated with the boundary of the uplifted region. This boundary is probably broad and diffuse consisting of slightly folded strata and some shear fracturing. There is no evidence indicating that uplift though localized permitted leakage of radioactivity from the immediate cavity environment.

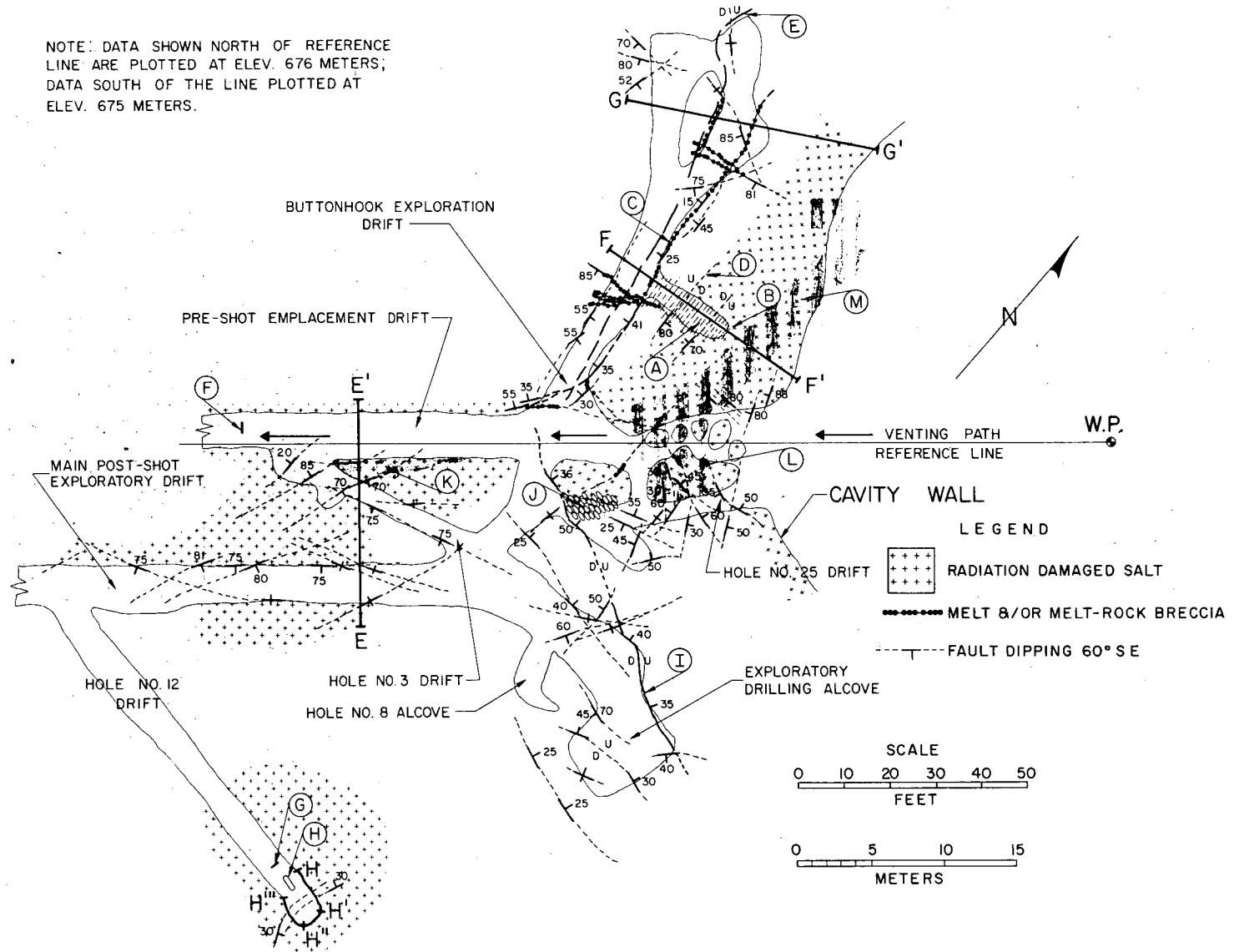
4.2 MELT AND GAS INJECTED FROM THE CAVITY INTO FRACTURES

Irradiation of rock salt results in distinctive yellow, blue, and purple coloration. For this reason, areas where radioactive gases were able to permeate are detectable even though radiation levels in some instances were near background at the time of exploration. Molten salt injected into cracks from the cavity characteristically is black and contains varying amounts of radioactivity. Using these color criteria, it was observed that above the working point, both gases and slightly radioactive melt permeated a distance of 38 m from the working point. This is rather surprising since a zone of greatly increased permeability extends vertically to a distance of about 105 m. Because of the infrequency of melt injections

LEGEND - Fig. 4.3

- A. Echelon tension fractures resulting from movement on major thrust fault. Probably extend full length of "buttonhook drift."
- B. Voids encountered at this location.
- C. Major thrust fault associated with closure of the "buttonhook drift."
- D. Abrupt termination of radiation damage at tension fracture.
- E. Approximate postshot boundary of left rib of "buttonhook" indicated by extent of melt and rock breccia.
- F. Approximate extent of major tunnel closure.
- G. Encountered water leakage from polyhalite #94 from this point to end of drift.
- H. Location of accelerometer that failed at 16 msec.
- I. Major overthrust fault with maximum observed displacement of 3 m (see Fig. 4.6a).
- J. Postshot location of sand bags in hole #25 alcove.
- K. Sheet of radioactive melt injected along a parting of clay beds.
- L. Preshot location of hole #25 alcove.
- M. Preshot location of "buttonhook drift."

NOTE: DATA NORTH OF REFERENCE LINE ARE PLOTTED AT ELEV. 676 METERS;
 DATA SOUTH OF THE LINE PLOTTED AT ELEV. 675 METERS.



-43-

Fig. 4.3 Rock deformation revealed by postshot mining - plan view.

and radiation-damaged salt encountered in exploration of this region, the relatively short vertical extent of these injections above the working point, and since the amount of radioactivity in the injected melt is much lower than melt encountered within the cavity; it is concluded that the open fractures communicating with the cavity developed early during the dynamic growth period. Injection at this time (10-100 msec) is likely because good physical mixing between the molten rock and the vaporized fission products would not yet have occurred.

In the equatorial region beyond the cavity, melt was observed as far as 40 m from the working point, and evidence of gaseous injection was observed as far out as 65.5 m. These distances refer to melt and gas injections that are believed to be unrelated to the vent path down the line-of-sight emplacement drift. Melt was injected into a clay parting along the line-of-sight emplacement drift to a distance of 58 m from the working point, and melt was also in the drift as far away as the concrete block stemming (Fig. 1.2). Cracks from this drift were also permeable to gases. Figure 4.3 shows the fracturing and the distribution of radiation-damaged salt and melt injection in this equatorial region.

Preshot hole #12 was explored to recover an instrument that failed at 16 msec (Reference 6) following the explosion. It was found to have been located in a region of anomalously large rock deformation with accompanying radiation damage in the salt and water leakage (Fig. 4.3) indicating permeable communication with the cavity. The

early failure of the instrument, coupled with the intense local deformation and its associated permeability communicating with the cavity, indicates that the fracturing started at about 16 msec, or immediately following the passage of the compressional shock wave. The cross section H-H''' (Fig. 4.4) located in plan in Fig. 4.3 is a detailed map of the deformation at the end of the hole #12 drift.

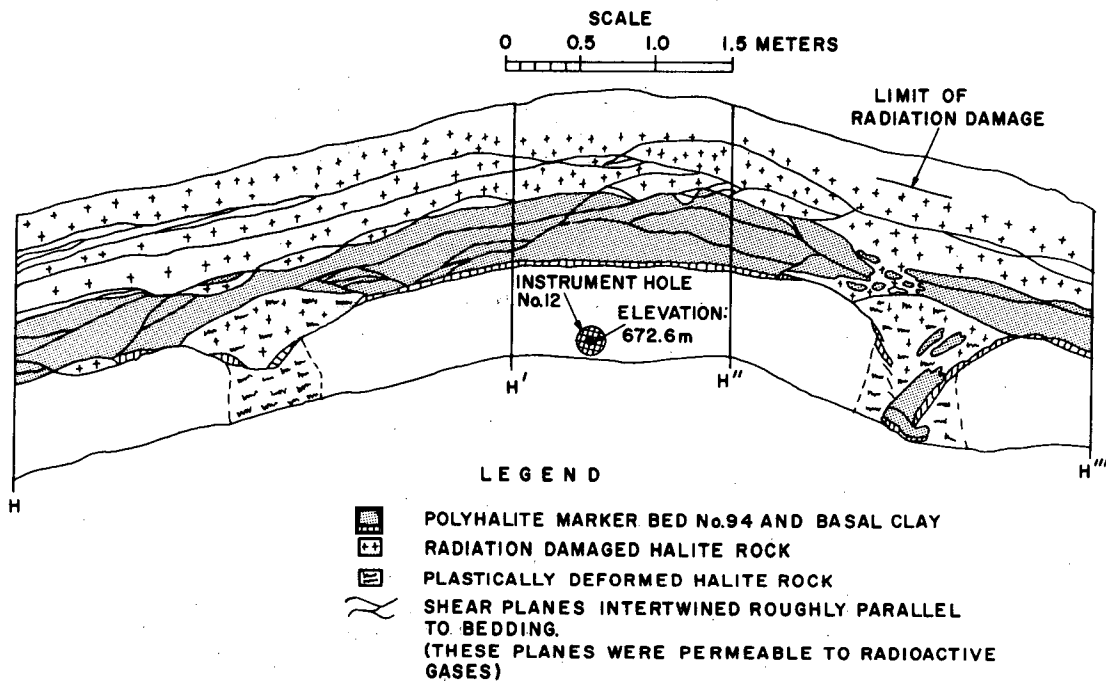


Fig. 4.4 Vertical section H-H''' showing deformation at end of hole #12 drift (see Fig. 4.3 for plan view).

Note the local downward motion of rock unit #93 through and mixed with that of the lower rock unit #94. This is very intense deformation at a distance of 65 m and compares with the intensity of deformation associated with closure of the "buttonhook" drift at a distance of about 30 m from the working point. The possible existence of a

natural cavity in the salt near the instrument location that was collapsed by the shock wave could be the explanation of this deformation. Such cavities are known to occur in the Salado formation (C. Jones, verbal communication) and are generally brine-filled. Figure 4.5 also shows the anomalously large radial displacements in that region.

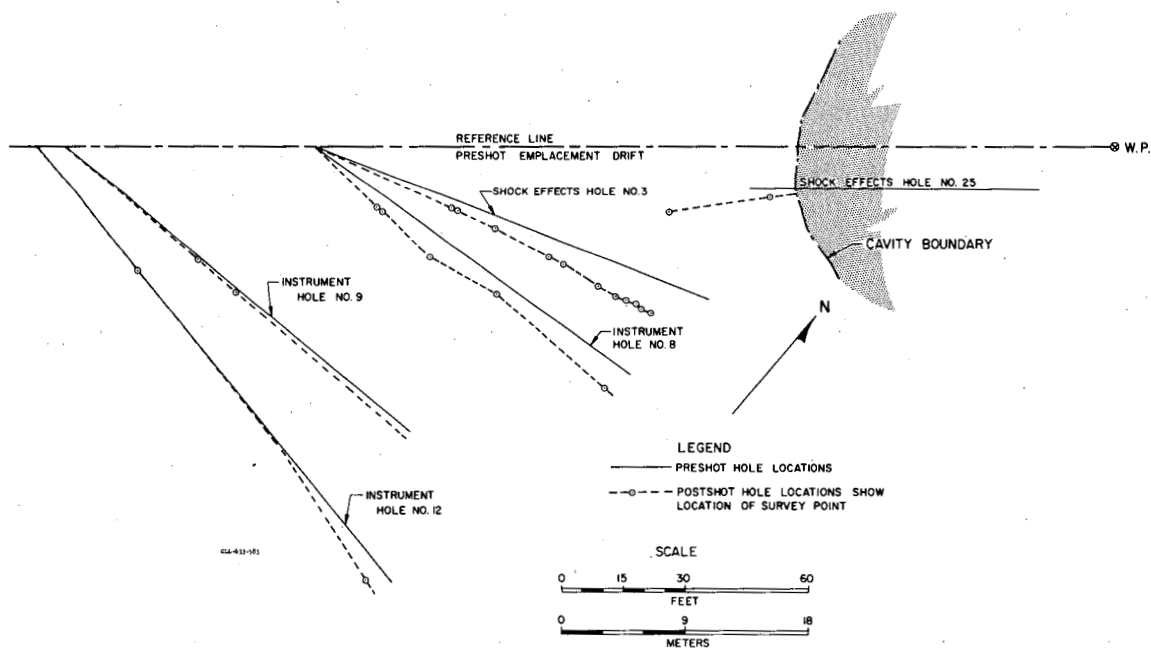


Fig. 4.5 Displacement of underground instrument and shock-study sample holes - plan view.

Exploration along the postshot location of the "buttonhook" drift, Fig. 4.3, encountered nonradioactive melt that was injected into the open drift and was then caught up in the rock motions associated with the drift closure. This relationship again supports the thesis that melt and possibly some radioactive gases escaped from the cavity

primarily during dynamic cavity growth. An exception, of course, is melt and gases that vented into the emplacement drift.

Below the shot point, neither melt samples, radiation-damaged salt, nor radiation levels above background, were noted further than 25 m from the working point or 6 m beyond the cavity edge.

4.3 DEFORMATION SURROUNDING THE CAVITY

Fractures resulting from the expanding cavity produced by the explosion and subsequent fracture development associated with unloading of the compressed rock can be grouped into the following four general categories:

- (1) Radial tension cracks emanating from the cavity;
- (2) Peripheral faults with planes that generally parallel the cavity boundary;
- (3) Bedding plane faults;
- (4) Near vertical joints primarily in the vicinity of preshot emplacement drifts.

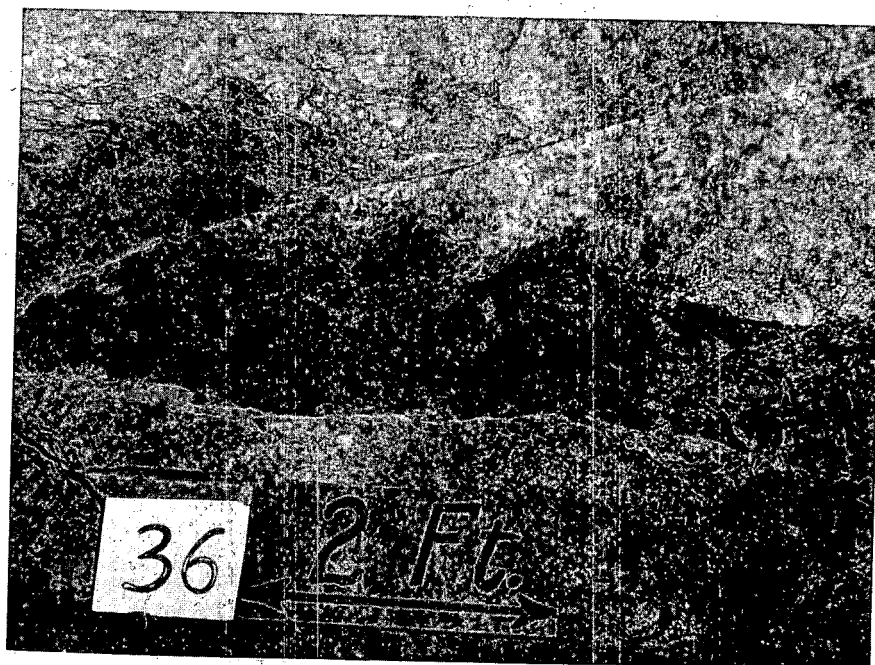
Figure 4.3 shows the projection of the traces of major faults, and joints at the elevations of 674.8 and 675.7 m that were revealed during mining exploration. Figure 2.1 is a reflected ceiling plan of the interior of the cavity showing the traces of major radial cracks. These cracks (type 1) occur with a frequency of about one every 4 or 5 m at the equator of the cavity and extend to a distance laterally and above the cavity of about 38 m. These are the cracks containing

injected melt (see Fig. 4.3 in the region of the "buttonhook drift" and the vertical section Fig. 2.2).

Also shown in these two figures are the curved peripheral faults. Below the shot point in drill holes B and C, the peripheral faults (type 2) are inferred from the attitude of fault planes in the core relative to the orientation of bedding planes. In the vicinity of the drill alcove (Fig. 4.3), this type of faulting grades into overthrust faults that further grade into horizontal bedding-plane slips along clay seams. Figures 4.6a and b shows examples of this kind of faulting. The throw or differential motion between blocks was measured to be 2.5 to 3.0 m across the fault marked (I) in Fig. 4.3. This was the largest fault observed; most differential motions are on the order of 0.5 m or less. This peripheral type of faulting does not contain melt injections and is probably formed after cavity growth when unloading or rebound adjustments to the stressed rock are likely to take place. Associated with these curved faults emanating from the region below the cavity is a gentle upwarping of the strata in the equatorial region. Marker bed #94 which was located a few meters below shot point became uplifted from its preshot elevation out to a distance of about 64 m. Beyond that point, the vertical displacement is not measurable. In the drill alcove polyhalite marker bed #94 was uplifted from 0.3 to 0.6 m instead of being depressed. This bed was located below the working point elevation prior to the explosion (see Fig. 2.1).



(a)



(b)

Fig. 4.6 Typical faults produced by the explosion:

The near-vertical joints are primarily associated with deformation in the rock near the line-of-sight portion of the emplacement drift. These joints form two distinct sets that intersect each other in a criss-crossed or trellis pattern. At a distance of 60 m from the shot point, the joints intersect the line of the drift at an angle of about 20° . Close to the cavity edge this angle has increased to 75° . Figure 4.3 shows some of the major joints mapped and Fig. 4.7 is a schematic drawing illustrating the trellis pattern of the joints and fractures associated with the line-of-sight drift. If this idealized

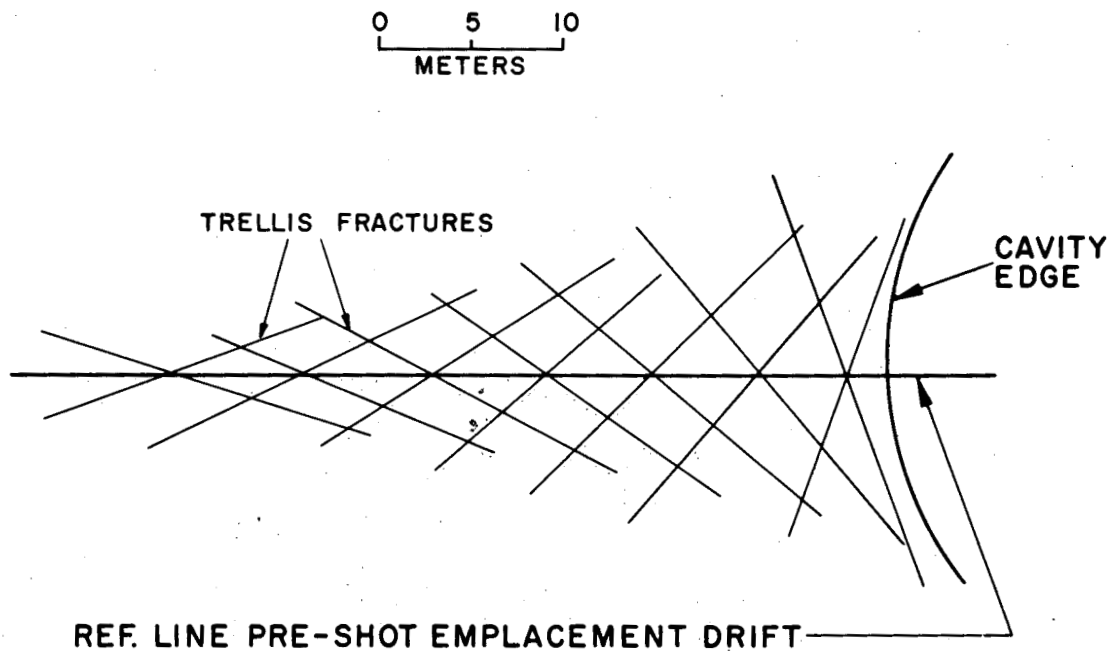


Fig. 4.7 Plan schematic of trellis fracture pattern associated with deformation along the line-of-sight emplacement drift.

interpretation is correct, it indicates that the rock bounding the drift failed in shear as the compressional wave passed and subsequent cavity growth distorted these weak zones.

4.4 DEFORMATION OF THE PRESHOT EMPLACEMENT DRIFT

In addition to the trellis pattern of fractures associated with the deformation of the line-of-sight portion of the emplacement drift, the drift was noticeably constricted by plastic deformation. Cross section E-E' (Fig. 4.8) located in plan on Fig. 4.3 shows the approximate size of the postshot emplacement drift at 53.3 m from the working point compared to its preshot cross section. At this distance, the drift apparently squeezed nearly shut prior to venting and was

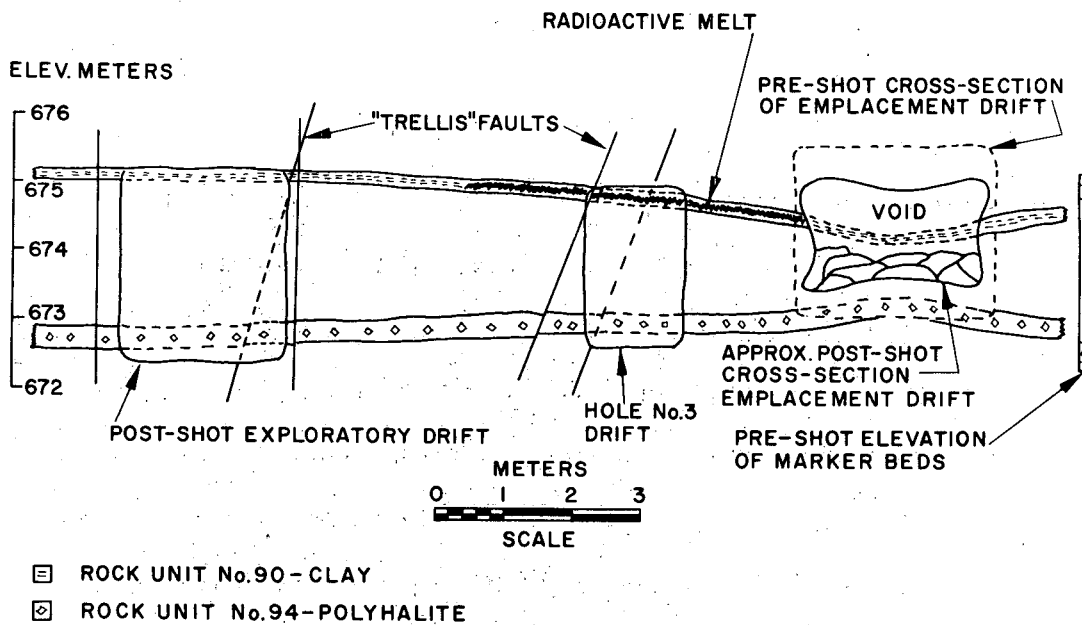


Fig. 4.8 Vertical section E-E' showing partial closure of preshot emplacement drift (see Fig. 4.3 for plan view).

then blown open to its final shape when venting occurred (see discussion on Venting - Chapter 5).

The curved or "buttonhook" portion of the emplacement drift sealed effectively and was not involved in the cavity venting process. The explored portion of this drift was tangential to the shot point rather than radial (as was the emplacement drift in the previous discussion), and the nature of tunnel closure was quite different. In the line-of-sight drift, ineffective closure was accomplished by plastic flow and slippage along the trellis fractures. In the "buttonhook" portion of the drift, the radial component of the outward moving, compressional shock wave met the drift at a right angle and virtually slammed one wall into the other. More precisely, the closure was accomplished by the movement of a wedge-shaped block into the open drift. The boundaries of this major block are partly controlled by clay seams in the rock that appear to have lubricated the movement of the major block. Figure 4.9 shows two cross sections illustrating the detailed structure of the deformation; their locations in plan view are marked in Fig. 4.3.

In the vicinity of Section G-G', radial cracks following the compressional shock wave opened up, allowing superheated melt to enter the drift prior to its closure. Here, the melt was mixed and trapped with the rock moving to seal off the drift and it formed the matrix of a melt-rock breccia. As it was injected into the drift, the melt encountered lead bricks and wood in an instrument alcove

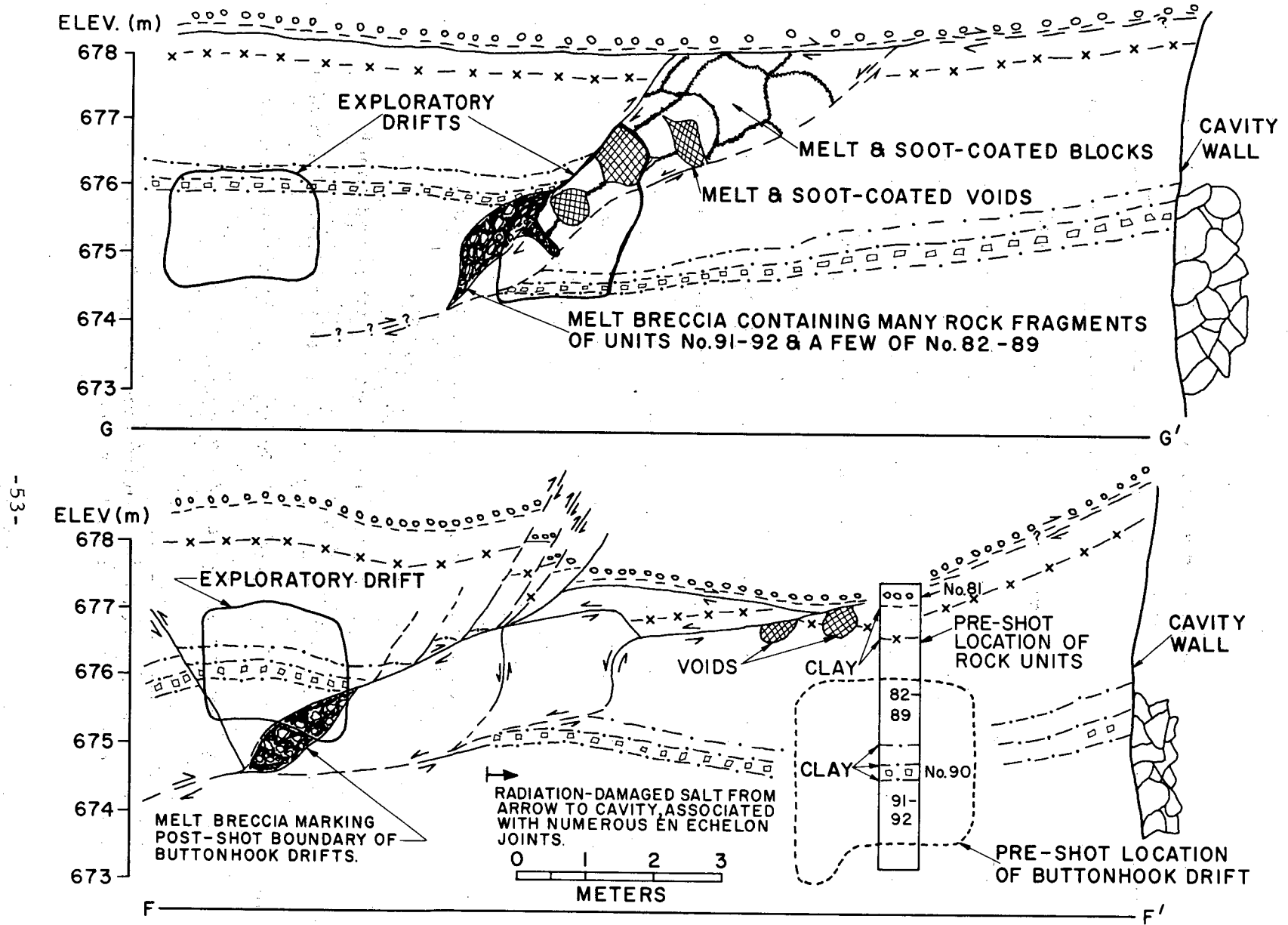


Fig. 4.9 Vertical sections F-F' and G-G' showing closure of "buttonhook drift" (see Fig. 4.3 for plan view).

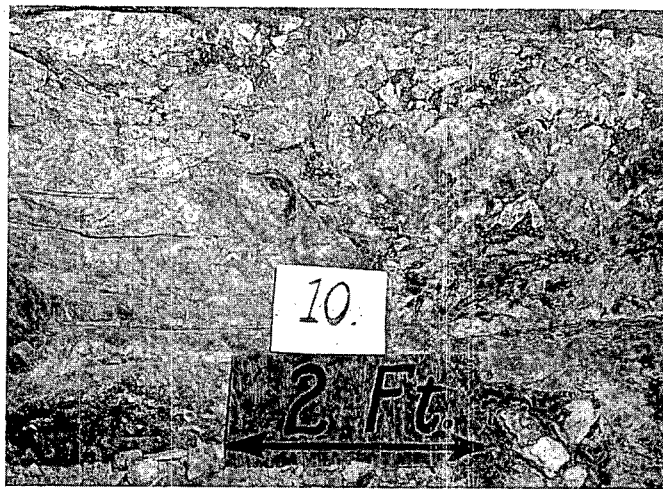
off the drift. The lead melted and the wood burned mixing with the salt-melt breccia. Analyses of the melt breccia shown in Fig. 4.10a, b, and c, indicate that lead combined with sulfur and chlorine from the melt to form galena (PbS) and laurionite ($\text{Pb}[\text{OH}]_2 \cdot \text{Pb}[\text{Cl}]_2$) (Reference 10). The laurionite was probably formed by the reaction of water dissolved in the salt melt with PbCl_2 . The sulfur necessary to combine with the lead was probably released by a reduction of sulfates associated with the molten salt. Hydrocarbons from the burning wood created a reducing atmosphere. An alternative explanation of the formation of the melt breccia is that it was produced locally in the drift by extremely high pressures and temperatures developed from the dynamic conditions of closure. The hypothesis of melt injection from the cavity (even though it is nonradioactive) is most consistent with the relationships observed. Some of these relationships are as follows:

1. Voids in the same region are coated with a mixture of soot, lead, and fused salt (see Section G-G' of Fig. 4.9);
2. In the breccia, insulation was still on wires and shock-produced Neumann bands* were not found in recovered steel samples that had been intimately mixed with the melt, indicating not nearly high enough pressures developed for melting;

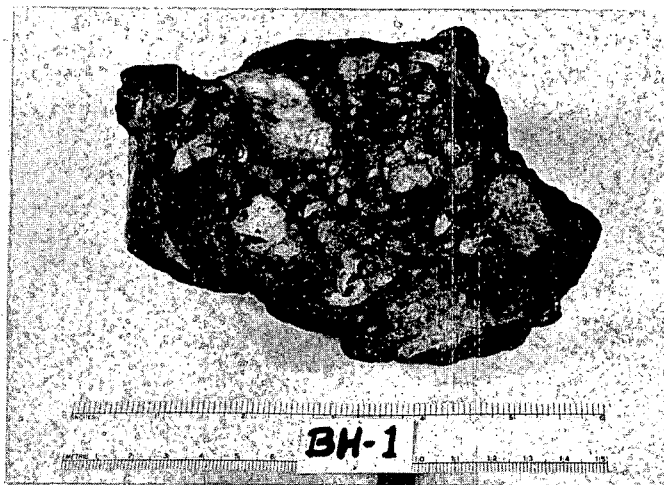
* Neumann bands are characteristic deformation features in steel caused by intense shock or impact loading.



(a)



(b)



(c)

Fig. 4.10 Intrusive melt breccia.

3. The percentage of melt, lead, and carbon in the breccia decreases from that located in the vicinity of cross section G-G' until absent from the breccia in the vicinity of cross section F-F'. Most of the matrix of the breccia is clay at that location.

4. As shown in Fig. 4.2, the preshot size of the drift was large where the alcove is located compared to the rest of the drift. This portion of the drift is also nearest the shot point and thus a logical place for cracks to open to melt injection from the growing cavity. If the melt was injected from the cavity into the cracks it would have had to follow immediately behind the compressional shock wave to get to the drift prior to closure. This would have occurred very early in the dynamic cavity growth period, while the cavity was small and the thickness of rock melted by the shock waves was relatively large (see Fig. 6.1a). Under these conditions poor mixing of the thick melt zone with the vaporized fission products would be likely and then explain the nonradioactive melt found in the drift.

CHAPTER 5

VENTING

5.1 THE VENTING PROCESS

Before developing a generalized interpretation of the venting processes a few pertinent facts and comments should be made:

1. As shown in Fig. 1.2, the neutron pipe was an open pipe that extended from the line-of-sight portion of the emplacement drift to the working point, thus introducing an inherent weakness in that region.
2. As shown in Fig. 4.9, the strata at the elevation of the emplacement drift were characterized by several clay seams of unusually low tensile strength. The clay is also very plastic, thus introducing another weakness.
3. In Section 4.4, it was mentioned that the squeezing action to close off the line-of-sight drift was ineffective compared to the tight closure of the drift where its walls were oriented tangentially, and not radially, to the shot point.
4. The block motion associated with the closure of the "button-hook" portion of the drift must result in the development of a boundary weak zone in the vicinity of the neutron pipe since south of this pipe (Fig. 1.2) there is no drift and radial rock movement would be less.
5. As shown in Figs. 4.3 and 4.8, radioactive melt was injected from the partly closed emplacement drift as a sheet into a parted clay

seam. Here the melt quenched and was not vesiculated indicating that it solidified under high pressure and, therefore, before the pressure drop that resulted from venting.

6. Venting occurred within 1 minute after the explosion (Section 1.4).

Between about 100 msec and one minute following the explosion, melt and gases were able to penetrate from the cavity into the closed but apparently permeable line-of-sight portion of the emplacement drift. This zone was especially weak for reasons 1 through 4, listed above.

The compressional wave produced by the explosion was reflected at the ground surface and returned to the cavity region as a rarefaction wave at about 320 msec. The intensity of this wave may have been great enough to put the rock into tension and cause parting of the clay seam (5 above). The permeability in this region would then be momentarily increased so that melt could be injected from the cavity into the parting and probably then into the more permeable or open drift beyond. When this occurred there was no longer much resistance to the cavity pressure and dynamic venting occurred. Melt, rock, neutron pipe, vent line, and most of what was in the drift were blown down the drift. Much debris piled up at the cement domino (Fig. 1.2). Radioactive melt was encountered as far as the concrete block stemming (Fig. 1.2). This stemming effectively throttled the dynamic venting and converted it to a leak. The drift

from the stemming into the cavity was probably near the overburden pressure of 1,200 psi. From the porous plug to the blast door, the pressure built up about 55 psi - sufficient to break one of two rupture disks in the blast door. From there, the blow-out continued up the shaft, through a filter and out into the open. The concrete block stemming performed as it was designed, to hold overburden pressure, but it was not gas-tight. Particulate radioactivity and violent venting were contained underground while steam and gaseous fission products escaped.

As was pointed out by E. Teller (Reference 11), the knowledge of how to control venting could be very important in recovering gaseous radioelements from a specially designed nuclear device. By accident, Gnome venting contributed greatly to this knowledge.

5.2 THE VENT PATH ENVIRONMENT

Following is a pictorial trip down the vent path from the shaft station down the emplacement drift and into the cavity:

Re-entry down the shaft 6 days following the explosion revealed very little damage. Hairline cracks were observed in several places in the concrete lining of the shaft between the surface and the top of salt. In general, these cracks correlate with the location of bedding planes between differing rock strata. Several below a depth of 146 m were seeping water. Others developed at joints in the cement. In the salt, there is an indication of slight parting at several places.

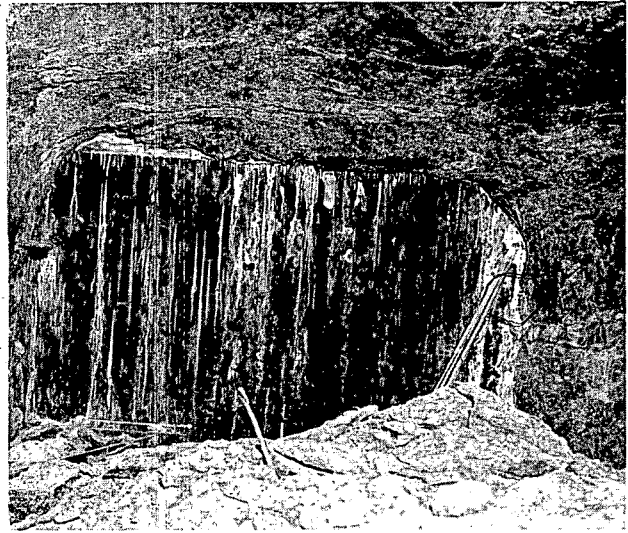
These were invariably associated with the bedding plane boundaries of clay seams and stringers of polyhalite and anhydrite - planes of essentially no tensile strength. In general, very little rock spalled from the shaft walls. At a depth of 326.1 to 327.4 m, about 2.5 m³ of material spalled from a very friable siltstone. The cage was lowered to within a few meters of the bottom station or drift level where the displacement of a metal safety railing stopped it. Fig. 5.1 shows the descent from the cage to the drift level and damage at the bottom station. Note the sag of the ceiling where spall occurred to a clay layer located 1 m above. Spall is the major damage in this region and most likely would not have occurred if that clay seam had been immediately above the drift. A 4.6-m-deep sump at the bottom of the shaft was full of water and the drift floor had up to 25 cm of standing water. Most of the water condensed from vented steam; however, some also seeped from the above-mentioned cracks. The salt exposed in these underground workings was colored due to the high radiation fields developed as a result of venting.

Figure 5.1b shows the "I" beam wall buttressing the concrete block stemming through which leakage occurred. It was determined that leakage was restricted to this region by pressurizing the Gnome cavity with air and surveying the vent path leakage.

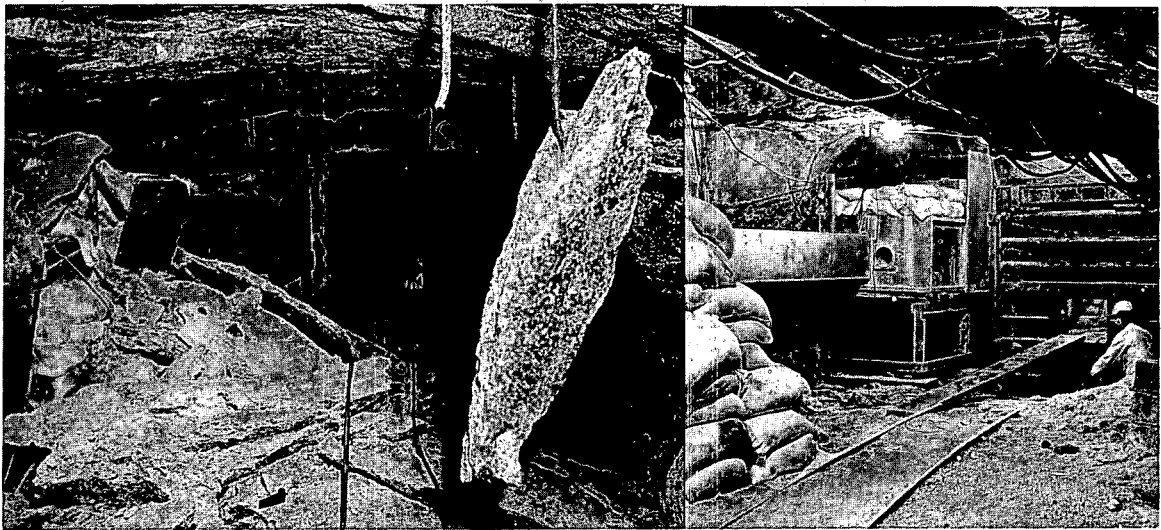
Figures 5.1c and d show a comparison of the preshot and post-shot condition of a portion of the drift between the concrete block stemming and the blast door, a distance about 270 m from the shot



(a)



(b)



(c)

(d)

Fig. 5.1 Deformation of emplacement drift near shaft.

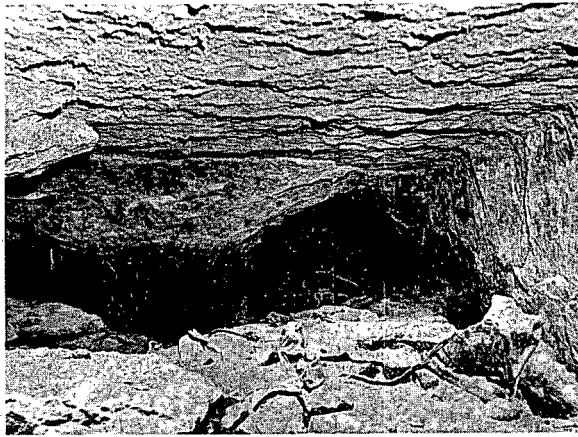
point. Again, most of the damage resulted from spall of the back to the clay seam.

Figure 5.2a shows the drift on the side of the concrete block stemming that experienced dynamic venting. Here, in addition to spall, there is evidence that material had been transported down the drift and had been subject to high pressure.

Figure 5.2b shows the collapsed neutron pipe in this region. Radioactive melt was also found that was ejected from the cavity. Radiation field levels were 1 to 3 R/hr (gamma radiation) six months following the explosion and the levels varied greatly, but generally decreased toward the cavity. Readings were generally between 1 R/hr and 100 mR/hr in the drift.

Figure 5.2c shows the drift in the vicinity of crosscut 1 (Fig. 1.2) approximately 105 m from the shot point. Note the curved distortion of the back and the bent bars and straps. Also, considerable scour of the walls was observed testifying to the violent movement of debris down the drift.

Figure 5.2d shows the boundary of a shear zone that was encountered while excavating crosscut 2 (Fig. 1.2). In this zone shearing in a horizontal direction occurred along vertical planes striking parallel to the emplacement drift. It extends from the right rib of the drift into the wall rock about 3 m and is associated with the failure of a drill alcove excavated on the right rib of the emplacement drift. The drill alcove was a departure from the line-of-sight drift,



(a)



(b)



(c)



(d)

Fig. 5.2 Deformation of emplacement drift between shaft and cavity.

in that the walls were no longer line-of-sight to the shot point in the alcove. This apparently was a significant perturbation on the stress distribution associated with the compressional shock wave causing the rock beyond the alcove and adjacent to the emplacement drift to fail in shear.

Figure 5.3a shows the drift at a distance of about 41 m from the shot point near the end of the postshot location of the line-of-sight portion of the emplacement drift. Here the salt is pock-marked with many large etch pits caused by steam erosion. The smooth dark patch in the center of the picture is a pond of water that condensed from the vented steam and the white crust is re-crystallized salt left by evaporation of brine.

Figure 5.3b is a picture of a small portion of the breakthrough region between the cavity and the line-of-sight drift. It is possible to crawl from the cavity through to the drift.

Figure 5.3c is a view from inside the Gnome cavity looking toward the portal to the vent path at the cavity wall.

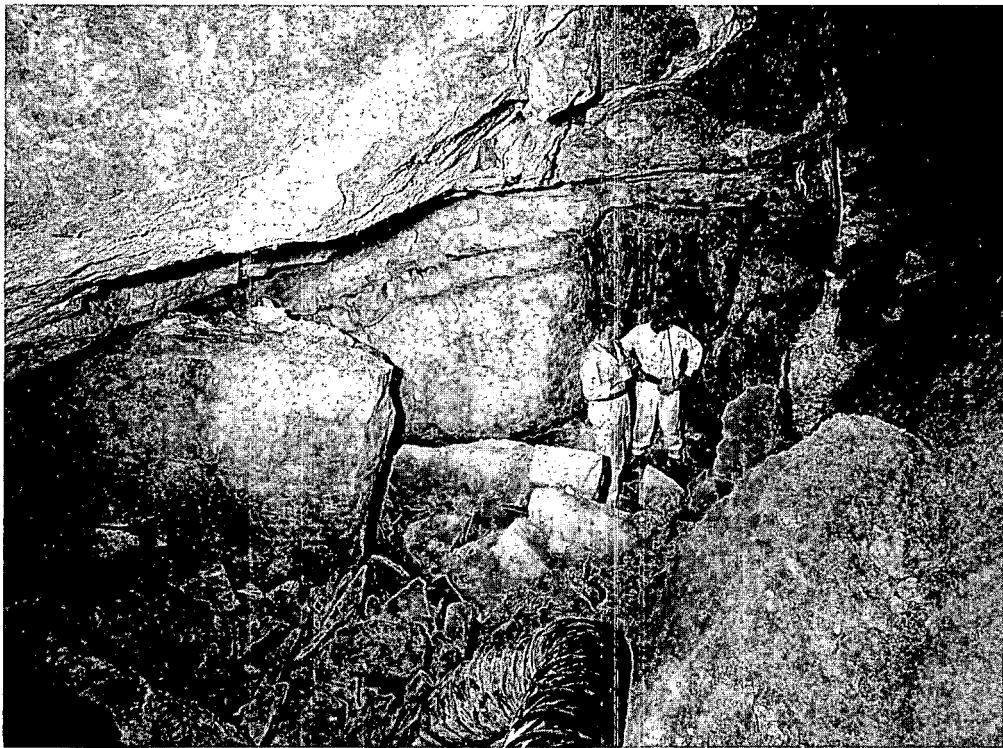
Figure 5.4 is a view of the cavity interior; the arrow points to a man for scale. The stalactites resulted from the evaporation of brine introduced during re-entry drilling.



(a)



(b)



(c)

Fig. 5.3 Vent path.

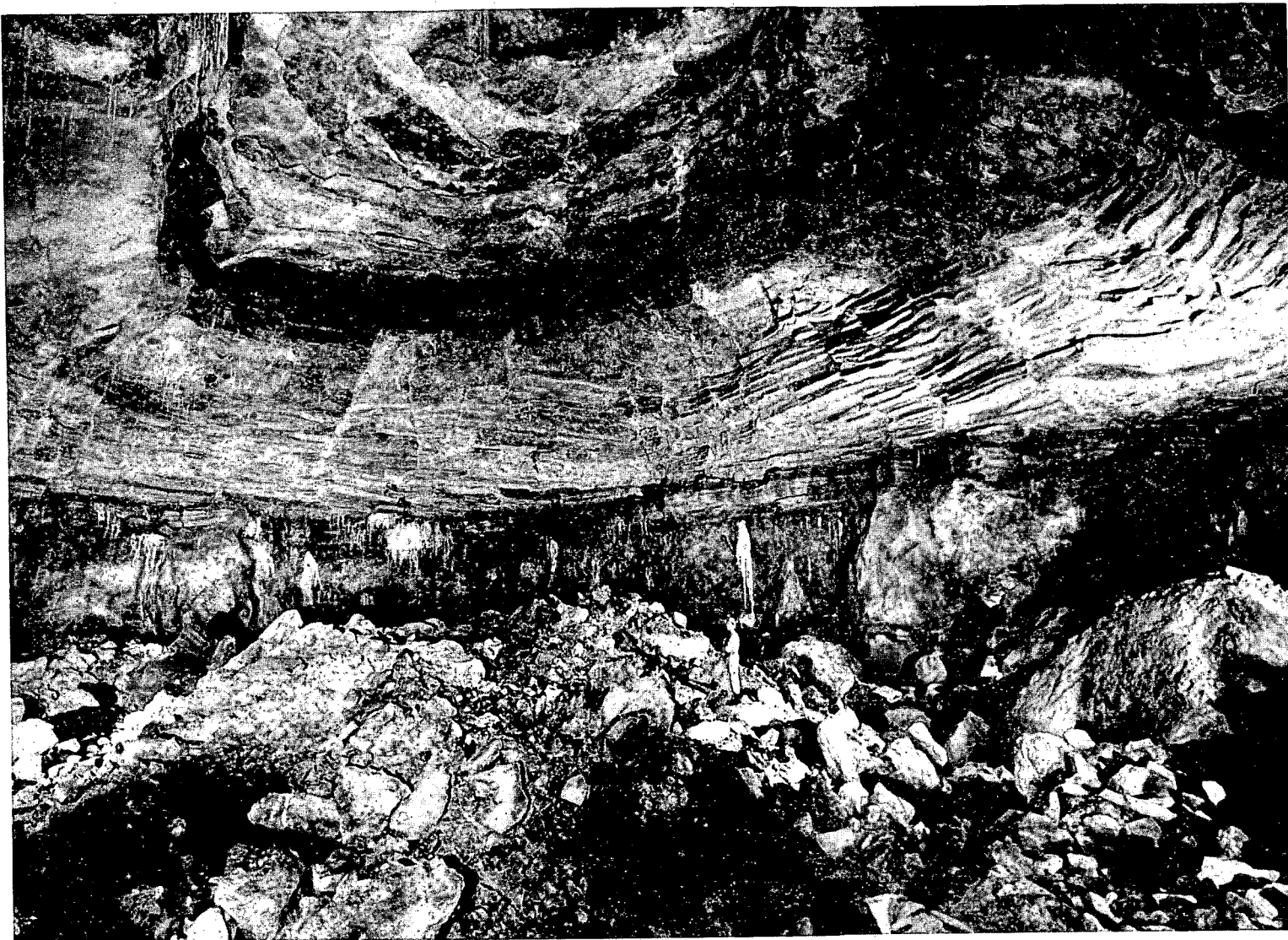


Fig. 5.4 View of interior of the Gnome cavity. Note size of man.

CHAPTER 6

AN INTERPRETATION OF THE EXPLOSION DYNAMICS

The description of the environment created by the Gnome event and the interpretations of processes leading to the observed results have been rather arbitrarily compartmentalized for the purposes of presenting the data. Actually, the period of cavity growth is about 100 msec, the accumulation of the melt and rubble at the base of the cavity was completed after a few minutes, and venting was complete in about 24 hours. Thus, the environment described resulted from very dynamic conditions and the observed effects are greatly inter-related. In order to convey some feeling for the development of the environment observed, a sequence of schematic illustrations have been prepared re-constructing the growth of the cavity as a function of time (Fig. 6.1). The illustrations are, of course, idealized; guidance for the temperature and pressure of the cavity gas was obtained from calculations made by Fred Seidl and Arturo Maimoni of LRL. These are order-of-magnitude approximations.

Figure 6.1a shows the cavity at about 3 msec and Fig. 6.1b at about 30 msec. When the nuclear device explodes, it creates an expanding plasma of extremely high temperature and pressure on the order of a few million degrees Celsius and several million bars. The plasma expands and slams into the confining rock, creating a supersonic compressional shock wave intense enough to vaporize

LEGEND - Fig. 6.1

- 1 Working Point - center of the nuclear explosive device.
- 2 Vaporized and ionized rock and device material.
- 3 Rock fused by supersonic compressional shock wave.
- 4 Location of rock strata.
- 5 Outgoing compressional shock wave.
- 6 Radial cracking and melt injection.
- 7 Rarefaction wave returning from ground surface.
- 8 Zone of rock that breaks up and "blows off" cavity surface.
- 9 Rock from 8 mixes with melt 3 and begins to accumulate a "puddle" at cavity base.
- 10 Return of rarefaction wave 7 leads to slight cavity growth and uplift of ceiling.
- 11 Fractures associated with uplift of cavity ceiling.
- 12 Extension of radial fractures and further melt injection.
- 13 Bedding plane partings in rock strata.
- 14 Probable time of venting from cavity into emplacement drift.
- 15 Melt and rock breccia - "puddle."
- 16 Rubble from ceiling collapse.

Figure	A	B	C	D	E	F
Time	~ 3 msec	~ 25 msec	~ 300 msec	~ 1 sec	~ 1 min	~ 5 min
Cavity Temperature (°C)	~ 100,000	~ 20,000	~ 4,000	~ 2,000	~ 1,000	~ 500
Cavity Pressure (bars)	~ 400,000	~ 300	~ 80	~ 40	~ 20	~ 5

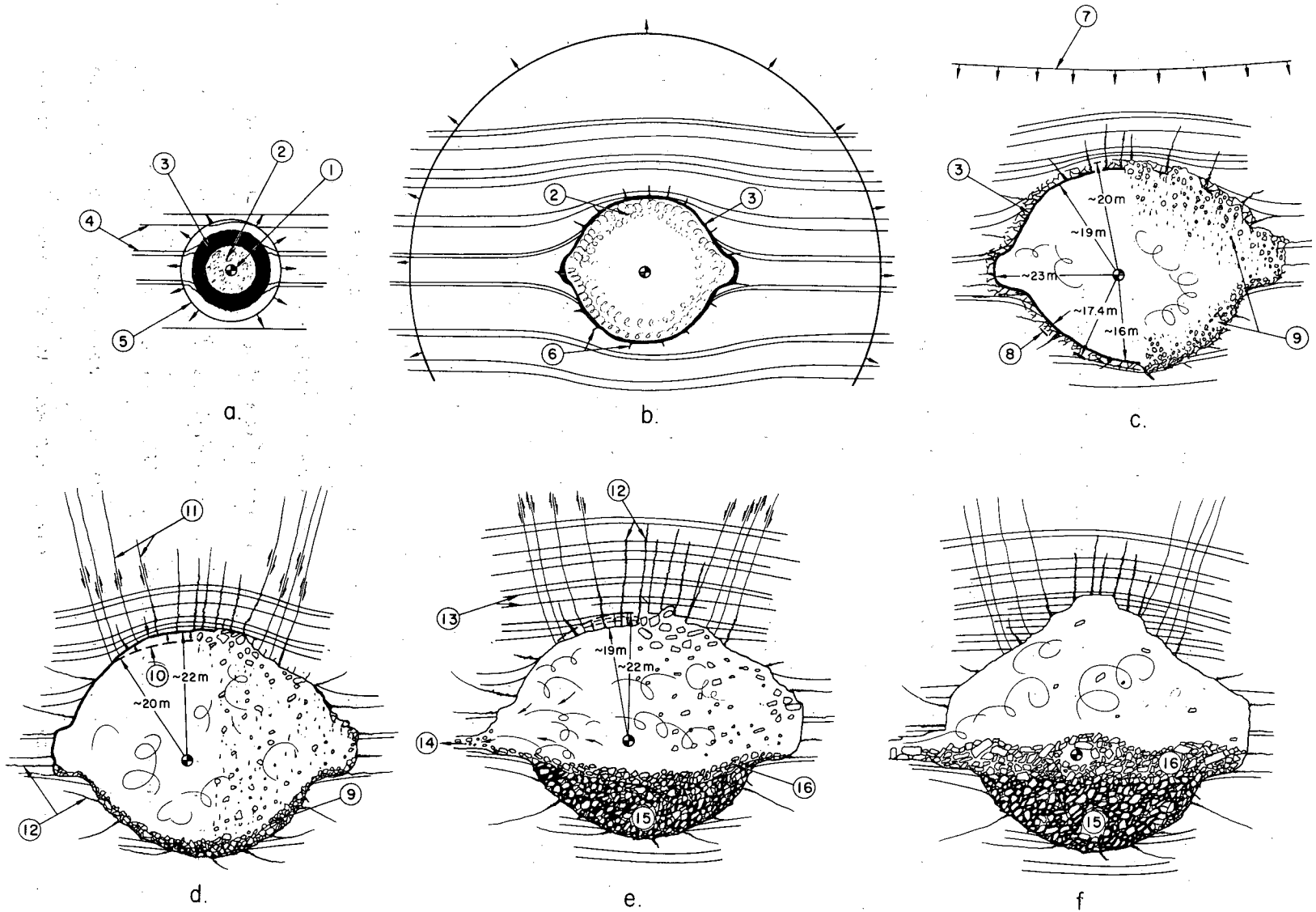


Fig. 6.1 Schematic vertical sections showing cavity development.

rock for some distance and then melt it for a further distance (about 7 m in the case of Gnome). The shock wave moves out, compressing the rock and decreasing in intensity with distance. It soon becomes a wave moving at the sonic velocity of the rock. The growth of the cavity follows behind the compressional wave and expands because of the driving force of the gas until the internal pressure is balanced by the resisting overburden pressure. At about 100 msec the expansion of the cavity is complete and the compressional shock wave has travelled a distance of about 475 m horizontally and about 300 m vertically (Reference 6). In the case of Gnome, it appears that the force resisting cavity growth in the direction parallel to the bedding planes in the rock was less than in the direction normal to these planes; this led to the development of the bulge in the equatorial region of the cavity. During this time period, radial tensional cracks opened up permitting the injection of melt and possibly some gas from the cavity. Generally, the injected melt contains little or no radioactivity because of poor mixing with the vaporized fission products.

As the expanding cavity comes to rest, the lining of fused rock flows and rains under the influence of gravity. This brings the melt into intimate contact with the condensing radioactive vapor and traps much of the fission debris. Near the end of cavity growth (Fig. 6.1c), "blow-off" of the cavity wall rock occurs resulting in rather intimate mixing of cooler rock and rapidly dropping temperatures inside the cavity. Since molten salt is about as fluid as water,

it fills most of the pore spaces in the lower hemisphere that developed as the wall rock breaks up and is quenched where in contact with the cooler rock. The rain of rock and melt creates a "puddle" at the base of the cavity where the nongaseous fission products are trapped (Fig. 6.1d and e).

While the puddle is forming another important event occurs - the arrival of the rarefaction wave from the ground surface. This wave tends to put the rock into tension, or at least decompression, and provides one mechanism for relief of the compressed and stressed rock and also slight further expansion of the cavity if its pressure then exceeds the resisting pressure of the confining rock (Fig. 6.1d). While the rarefaction wave travels from the ground surface back to the cavity region, the upper few hundred feet of rock spalls, and at Gnome the free-flight period for the ground surface lasted from 157 msec to a little over 1 second following the explosion (Reference 6). This allowed time for the rarefaction wave to return to the cavity and localized uplift to develop in the rock overlying the cavity, while the overburden weight decreased because of spall of the upper rock layers. Also at this time, compressed rock surrounding the cavity was unloaded and adjustments were made - most notably the upward arching of the rock surrounding the cavity. A most probable time for venting would be at this time, when the rarefaction wave arrives, tending to part the rock strata and provide an escape path from the cavity to the open drift. The

rarefaction wave would also shake the cavity which might disrupt its stability and initiate some roof collapse.

Figure 6.1e shows the cavity after venting. Melt and rubble are still accumulating in the base of the cavity. The uplifted rock sags or partly drops back toward the cavity, leaving partings along the bedding planes between rock strata, and the ceiling of the cavity collapses.

In Fig. 6.1f, the "smoke is clearing," and the envisioned picture is very similar to that observed on re-entry exploration.

REFERENCES

1. Hydrologic and Geologic Studies, Project Gnome Report PNE-130F, U. S. Geologic Survey, September 25, 1962.
2. Hoy, R. B. and R. M. Foose, "Earth Deformation from a Nuclear Detonation in Salt," PNE-109P, Stanford Research Institute, March, 1962.
3. Randolph, P. and G. Higgins, "Various Papers Giving Some Early Gnome Results," Lawrence Radiation Laboratory (Livermore, California) Rept. UCID-4423, January 19, 1962.
4. Higgins, G. H., D. E. Rawson, and W. Z. Wade, "Chemical Reactions Induced by Underground Nuclear Explosions," Lawrence Radiation Laboratory (Livermore, California) Rept. UCRL-5882 Rev., 1961.
5. Nathans, M. W., "Isotope Program," PNE-102F (to be published).
6. Weart, W. D., "Particle Motion Near a Nuclear Detonation in Halite," PNE-108P, 1961.
7. Holmes and Narver, Field Drawing #F-01371, December 27, 1961.
8. Gard, L. M., "Lithologic Log of the Recover-Hole Core, Project Gnome," U. S. Geol. Surv. Tech. Letter, Gnome 1, November, 1961.

REFERENCES (Continued)

9. Sterrett, T. S., "Summary of Drilling Data for USGS Hole 6 and 7, Project Gnome," U. S. Geol. Surv. Tech. Letter, Gnome 14, September, 1962.

10. Gard, L. M., "Some Geologic Effects of the Gnome Nuclear Explosion," U. S. Geol. Surv. Tech. Letter, Gnome 15, October, 1962.

11. Teller, E., "Plowshare," Nuclear News, Vol. 6, No. 3, March, 1963.

APPENDIX A

DESCRIPTION OF ROCK STRATA SURROUNDING THE GNOME EVENT

The rock units described below indicate the variability of strata in the vicinity of the Gnome event, and Figs. 2.1, 2.2, 2.3, 4.4, 4.8, and 4.9 are maps showing the relations of certain of these units to other features produced by the explosion. The descriptions are condensed from the USGS Lithologic Log of the AEC Recovery Hole (Tech. Letter: Gnome-1). The unit numbers were derived by assigning number 1 to the first unit described in this log, at a depth of 304.8 m, and then continuing consecutively through the last unit described, No. 135, which ends at 396.2 m. In the listing below, units which are referred to in this report are grouped together for purposes of simplicity and clarity.

<u>Unit Nos.</u>	<u>Preshot depth (m)</u>	<u>Description</u>
14 - 17	311.7 - 314.9	Clear halite rock with minor clay and polyhalite
18 - 20	314.9 - 316.1	Halite rock, clayey at top, 40% polyhalite in middle
21 - 26	316.1 - 317.3	Clear halite rock with considerable polyhalite and red clay near bottom
27	317.3 - 317.7	Polyhalite rock
28	317.7 - 320.3	Orange halite rock with minor polyhalite

<u>Unit Nos.</u>	<u>Preshot depth (m)</u>	<u>Description</u>
29 - 31	320.3 - 322.4	Halite rock, with several clay layers
32 - 34	322.4 - 323.9	Orange halite rock with thin polyhalite layer
35 - 37	323.9 - 325.4	Claystone and clayey halite rock
38	325.4 - 328.4	Orange halite rock with minor polyhalite and silt
39	328.4 - 328.9	Clayey halite rock
40 - 41	328.9 - 331.1	Reddish halite rock with minor clay and polyhalite
42	331.1 - 332.9	Polyhalite rock, with halite and clay layers
43	332.9 - 336.5	Halite rock with minor polyhalite
44	336.5 - 337.2	Clayey halite rock
45 - 51	337.2 - 339.5	Halite rock with minor silt and polyhalite
52 - 60	339.5 - 343.1	Polyhalite, halite, anhydrite and clay layers
61	343.1 - 344.3	Silty halite rock
62 - 64	344.3 - 345.9	Halite rock with clay and polyhalite
65	345.9 - 350.8	Halite rock with many thin layers of anhydrite
66 - 77	350.8 - 352.4	Halite rock with clay and polyhalite layers
78 - 80	352.4 - 357.2	Halite rock with considerable polyhalite and clay
81	357.2 - 357.7	Polyhalite rock (Marker Bed #120)
82 - 93	357.7 - 361.9	Halite rock with clay and polyhalite

<u>Unit Nos.</u>	<u>Preshot depth (m)</u>	<u>Description</u>
94	361.9 - 362.3	Polyhalite rock (Marker Bed #121)
95 - 98	362.3 - 366.1	Orange halite rock with minor polyhalite and clay
99 - 104	366.1 - 366.9	Halite, polyhalite and clay layers
105	366.9 - 369.6	Orange halite rock with minor polyhalite and clay
106 - 107	369.6 - 370.9	Halite rock with minor polyhalite
108	370.9 - 374.7	Pinkish-gray halite rock with 30% clay
109 - 110	374.7 - 376.4	Clayey halite rock
111 - 114	376.4 - 381.6	Union anhydrite bordered on top and bottom by polyhalite
115 - 120	381.6 - 385.5	Clayey halite rock with gray clay seams
121 - 123	385.5 - 389.2	Orange halite rock with minor polyhalite
124 - 126	389.2 - 390.8	Claystone and halite rock
127 - 133	390.8 - 393.8	Gray to orange halite rock with 1-2% polyhalite and 5-10% clay

APPENDIX B

APPROXIMATE PRESHOT CHEMICAL COMPOSITION
OF THE ROCK FUSED AND VAPORIZED BY
THE GNOME EVENT

The following percentages represent average values obtained from chemical analyses of preshot drill-hole core samples weighted to represent the zone of fused and vaporized rock. Composite samples were analyzed representing a sphere of rock surrounding the explosion center of 8.5 m radius.

Si	0.185%	K	1.43%
Cl	55.4%	Fe	0.04%
Ca	1.40%	Al	0.071%
Mg	0.65%	Na	35.0%
SO ₄	6.38%	C	0.094%
		H ₂ O	~ 1.5%

APPENDIX C

ASSUMPTIONS INHERENT IN THE TREATMENT OF THE PERMANENT DISPLACEMENT DATA

The equation used to analyze the permanent displacement data is: $R_c = (R_f^3 - R_i^3)^{1/3}$. This equation is based on the relationship:

$$\frac{4}{3} \pi R_c^3 = \frac{4}{3} \pi R_f^3 - \frac{4}{3} \pi R_i^3$$

where:

R_c = Radius of theoretical cavity void,

R_f = Postshot radial distance of point p from working point, and

R_i = Preshot radial distance of point p from working point.

It assumes that the displacement of material is radial from the working point and that neither density changes nor faulting occur in the rock as it yields to the force of the expanding cavity. These assumptions are not true, however. Faulting was observed, and probably some permanent compaction of the rock, especially the clay units, did occur. Thus, cavity radii calculated by means of the foregoing equation are only approximations.

APPENDIX D

CAVITY VOID, RUBBLE, AND MELT VOLUME

CALCULATIONS

D.1 EXISTING CAVITY VOID VOLUME

The average planimetered area of three vertical sections of the existing cavity void is 795 m^2 . Assuming this void to be roughly hemispherical, the following relationship exists:

$$\frac{\pi}{2} R^2 = 795 \text{ m}^2 \quad \text{or} \quad R = 22.6 \text{ m},$$

where R is the radius of the hemisphere. The volume of the existing cavity is therefore:

$$\frac{2}{3} \pi (22.6)^3 = 24,180 \text{ m}^3$$

D.2 TOTAL VOLUME OF RUBBLE, MELT AND INTERSTITIAL VOID IN THE LOWER HEMISPHERE OF THE CAVITY

D.2.1 Volume of Rubble and Interstitial Void Above the "Approximate Upper Boundary of Melt" (Fig. 2.2). The average height and radius of this zone are 5.2 m and 22.9 m respectively. Assuming a cylindrical shape, its volume is

$$\pi (22.9)^2 (5.2) = 8,560 \text{ m}^3$$

D.2.2 Volume of Melt, Rubble, and Interstitial Void Below the "Approximate Upper Boundary of Melt." This zone is approximately a spherical segment with an average height of 12.2 m and

average radius at the upper melt boundary of 18.3 m. Its volume can be expressed as follows, using the formula for volume of a spherical segment.

$$V = \frac{\pi}{6} 12.2 [3(18.3)^2 + (12.2)^2] = 7,360 \text{ m}^3$$

Total volume of cavity rubble, melt, and interstitial void is therefore the sum of A and B or $15,920 \text{ m}^3$.

D.3 VOLUME AND MASS OF MELT

The average percentage of melt encountered by the underground drill holes is 27%. Using this percentage to represent the melt content of the spherical segment in D.2.2, the resulting melt volume is $1,980 \text{ m}^3$. The average bulk density of this melt is 1.6 g/cc. Therefore, its mass is:

$$(1,600 \text{ kg/m}^3)(1,980 \text{ m}^3) = 3.2 \times 10^6 \text{ kg}$$

D.4 TOTAL VOID VOLUME CREATED BY THE DETONATION

D.4.1 Void Volume Represented by the Porosity of the Melt.

The porosity of the melt is approximately 27% (bulk density = 1.6, natural state density = 2.2) and the total volume of the melt is $1,980 \text{ m}^3$. Therefore its vesicular void volume is:

$$(0.27)(1,980 \text{ m}^3) = 540 \text{ m}^3$$

D.4.2 Void Volume Representing the Interstitial Pore Space in the Rubble. Assuming a porosity of 28% for the rubble (excluding the melt which fills up a large amount of that space) the total void

volume of the rubble pile is:

$$(0.28)(15,920 \text{ m}^3) = 4,460 \text{ m}^3$$

A porosity of 28% was chosen because the Hardhat event in granite produced a rubble-filled chimney with this porosity. Subtracting the volume of the melt ($1,980 \text{ m}^3$), the resulting volume of rubble pore space is $2,480 \text{ m}^3$.

Total void volume created by the detonation is therefore the sum of the following volumes:

Cavity	24,180 m ³
Melt pore volume	540 m ³
Rubble pore volume	2,480 m ³
	<hr/>
	27,200 m ³

D.5 TOTAL VOLUME AND MASS OF RUBBLE

The volume of the rubble, obtained by subtracting the pore volume of the rubble ($2,480 \text{ m}^3$) and melt, including pore space, ($1,980 \text{ m}^3$) from the total volume of the rubble pile ($15,920 \text{ m}^3$) is $11,460 \text{ m}^3$.

Assuming a natural state bulk density of 2.2 g/cc, the rubble mass is:

$$(2200 \text{ kg/m}^3)(11,460 \text{ m}^3) = 25.2 \times 10^6 \text{ kg}$$

APPENDIX E

RUBBLE DISTRIBUTION

The total volume of rubble, exclusive of interstitial void, is roughly $11,460 \text{ m}^3$. Of this volume, approximately $5,300 \text{ m}^3$ is intimately associated with the melt in the lower hemisphere of the cavity. The remaining $6,160 \text{ m}^3$ blankets this region and contains very little melt.

The average theoretical cavity radius of the lower hemisphere, defined by permanent rock displacements, is approximately 16.2 m, and that defined by the extent of melt is 17.4 m. The difference of 1.2 m in these radii may represent the thickness of the shell of rock "blown off" the cavity walls at early times. Assuming this thickness to be roughly uniform around the cavity and assuming a cavity radius prior to "blow-off" of 18.7 m (the radius of a sphere of approximately $27,200 \text{ m}^3$ volume), the volume of the shell of blown-off rock is $5,600 \text{ m}^3$. Since this volume is very close to that of the rubble associated with melt, it is suggested that the bulk of the rubble in this region was blown off the cavity walls.

The average radius of the upper hemisphere of the cavity is approximately 22.9 m. A maximum early-time cavity radius of 18.7 m in this region is assumed. The 4.2-m difference in these radii represents the thickness of both collapsed and blown-off rock. Assuming a thickness of 1.2 m was blown off (as determined previously), a 3-m-thick shell of rock collapsed from the roof of the cavity. Cavity

profiles suggest this shell extended to an elevation of approximately 682 m or 7.9 m above the working point. The volume of this shell of collapsed rock can be approximated by the difference in volume of spherical segments with respective heights of 13.7 m (21.6 less 7.9 m) and 10.8 m (18.7 less 7.9 m), and basal radii of 25 m (scaled from Figs. 2.1 and 2.2) and 22.1 m. This results in a collapsed rock volume of $5,850 \text{ m}^3$, which compares favorably with the volume of rock overlying the melt zone.

TECHNICAL REPORTS SCHEDULED FOR ISSUANCE
BY AGENCIES PARTICIPATING IN PROJECT GNOME

AEC REPORTS

<u>AGENCY</u>	<u>REPORT NO.</u>	<u>SUBJECT OR TITLE</u>
LRL	PNE-101	Power Studies
LRL	102	Isotopes Program
ORNL	103	Design of Sequenced Gas Sampling Apparatus
LRL	104	Close-In Shock Studies
LRL	105	Stress Measurements with Piezoelectric Crystals
LRL	106	Post-Shot Temperature and Radiation Studies
LRL	107	Geologic Studies of the Tunnel and Shaft
SC	108	Particle Motion near a Nuclear Detonation in Halite
SRI	109	Earth Deformation from a Nuclear Detonation in Salt
USC&GS	110	Seismic Measurements from a Nuclear Detonation in Halite
SRI	111	Intermediate-Range Earth Motion Measurements
LRL	112	An Investigation of Possible Chemical Reactions and Phase Transitions Caused by a Nuclear Explosive Shock Wave
LRL	113	Resonance Neutron Activation Measurements
LASL	114	Symmetry of Fission in U^{235} at Individual Resonances
EG&G	115	Timing and Firing
WES	116	Design, Test and Field Pumping of Grout Mixtures
USWB	126	Preliminary Report of Weather and Surface Radiation Prediction Activities for Project Gnome; Final Analysis of Weather and Radiation Data
H&N, INC	127	Pre-Shot and Post-Shot Structure Survey

<u>AGENCY</u>	<u>REPORT NO.</u>	<u>SUBJECT OR TITLE</u>
RFB, INC	PNE- 128	Summary of Predictions and Comparison with Observed Effects of Gnome on Public Safety
SC	129	Monitoring Vibrations at the US Borax and Chemical Company Potash Refinery
USGS	130	Hydrologic and Geologic Studies
FAA	131	Federal Aviation Agency Airspace Closure
USPHS	132	Off-Site Radiological Safety Report
REE Co	133	On-Site Radiological Safety Report
USBM	134	Pre and Post-Shot Mine Examination

DOD REPORTS

<u>AGENCY</u>	<u>SUBJECT OR TITLE</u>
EG&G	Technical Photography of Surface Motion
STL	Shock Spectrum Measurements - Reed Gage
SC	Microbarographic Measurements
USGS	Study of Electric and Magnetic Effects
SC	Electromagnetic Waves from Underground Detonations
EG&G	Subsurface Electromagnetic Waves
SGC	Earth Currents from Underground Detonations
ERDL	Reflectance Studies of Vegetation Damage
SRI	Visual and Photographic On-Site Inspection
SRI	Seismic Noise Monitoring
ERDL	Soil Density Studies
TI	Geochemical and Radiation Surveys
USGS	Solid State Changes in Rock
EG&G	Radon Studies
C&GS	Intermediate Range Seismic Measurements
GeoTech	Long Range Seismic Measurements
USGS	Aeromagnetic and Aeroradiometric Surveys
ARA	On-Site Resistivity and Self Potential Measurements

ABBREVIATIONS FOR TECHNICAL AGENCIES

ARA	Allied Research Associates Inc. , Boston
EG&G	Edgerton, Germeshausen, and Grier, Inc. , Boston, Las Vegas, and Santa Barbara
ERDL	USA C of E Engineer Research and Develop- ment Laboratories, Ft. Belvoir
GeoTech	The Geotechnical Corporation, Garland
LASL	Los Alamos Scientific Laboratories, Los Alamos
LRL	Lawrence Radiation Laboratory, Livermore
SC	Sandia Corporation, Albuquerque
SGC	Space-General Corporation, Glendale
SRI	Stanford Research Institute, Menlo Park
STL	Space Technology Laboratories, Inc. , Redondo Beach
TI	Texas Instruments, Inc. , Dallas
USC&GS	Coast and Geodetic Survey, Washington, D. C. and Las Vegas
USGS	Geological Survey, Denver
WES	USA C of E Waterways Experiment Station, Jackson
FAA	Federal Aviation Agency, Salt Lake City
H&N, Inc.	Holmes and Narver, Inc. , Los Angeles
RFB, Inc.	R. F. Beers, Inc. , Alexandria
REECo	Reynolds Electrical and Engineering Co. , Las Vegas
USBM	U. S. Bureau of Mines, Washington, D. C.
USPHS	U. S. Public Health Service, Las Vegas
USWB	U. S. Weather Bureau, Las Vegas

DISTRIBUTION LIST - PROJECT GNOME

<u>AGENCY</u>	<u>NO. COPIES</u>	<u>AGENCY</u>	<u>NO. COPIES</u>
Oak Ridge National Laboratory Union Carbide Nuclear Company P. O. Box X Oak Ridge, Tennessee ATTN: J. W. Landry	1	Chief Air Force Technical Applications Center Washington 25, D. C.	6
Sandia Corporation Sandia Base P. O. Box 5800 Albuquerque, New Mexico ATTN: W. R. Weart	1	Chief Defense Atomic Support Agency Washington 25, D. C.	6
Stanford Research Institute P. O. Box 725 Menlo Park, California ATTN: R. B. Hoy	1	Commander Field Command, Defense Atomic Support Agency Sandia Base, Albuquerque, New Mexico ATTN: FCWT ATTN: FCTGS	8 2
Stanford Research Institute P. O. Box 725 Menlo Park, California ATTN: L. M. Swift	1	Armed Services Technical Information Agency (ASTIA) Arlington Hall, Virginia	2
U. S. Coast and Geodetic Survey Washington 25, D. C. ATTN: Mr. W. V. Mickey	1	Sandia Corporation Sandia Base, Albuquerque, New Mexico ATTN: Section 7250, Mr. A. D. Thornbrough	2
U. S. Coast and Geodetic Survey Washington 25, D. C. ATTN: Dr. Dean S. Carder	1	Space Technology Laboratories, Inc. Ramo-Wooldridge Corporation P. O. Box 95001 Los Angeles 45, California ATTN: Mr. James F. Halsey	1
U. S. Coast and Geodetic Survey Washington 25, D. C. ATTN: Mr. L. M. Murphy	1	U. S. Geological Survey Federal Center Denver 25, Colorado ATTN: Dr. George Keller and Mr. Karl Roach	2
Los Alamos Scientific Laboratory P. O. Box 1663 Los Alamos, New Mexico ATTN: G. A. Cowan	1	Edgerton, Germeshausen & Grier, Inc. 300 Wall St., P. O. Box 1912 Las Vegas, Nevada ATTN: Mr. R. A. Lusk	2
Edgerton, Germeshausen & Grier, Inc. 160 Brookline Avenue Boston 15, Massachusetts ATTN: Mr. F. I. Strabala	2	Director Mine Detection Branch Engineer Research & Development Laboratories Fort Belvoir, Virginia ATTN: Mr. S. E. Dwornik	2
U. S. Army Engineer Waterways Experiment Station Corps of Engineers Jackson Installation, Concrete Division P. O. Drawer 2131 Jackson, Mississippi ATTN: J. M. Polatty	3	Texas Instruments, Inc. Geosciences Division P. O. Box 35084, Airlawn Station Dallas 35, Texas ATTN: Mr. Hubert M. Rackets	2
Shell Development Co. 3737 Bellaire Blvd. Houston, Texas ATTN: Dr. Aaron J. Seriff	1	The Geotechnical Corporation P. O. Box 28277 Dallas 28, Texas ATTN: Mr. Ernest Stevens	2
University of California Lawrence Radiation Laboratory Livermore, California ATTN: Technical Information Division	25	U. S. Coast & Geodetic Survey Department of Commerce P. O. Box 267 Mercury, Nevada ATTN: Mr. Thomas H. Pearce	2
Assistant to the Secretary of Defense for Atomic Energy Department of Defense Washington 25, D. C.	1	U. S. Coast & Geodetic Survey Department of Commerce Washington 25, D. C. ATTN: Chief, Division of Geophysics	2
Chief Advanced Research Projects Agency Washington 25, D. C.	6	Allied Research Associates, Inc. 43 Leon Street Boston 15, Mass. ATTN: Dr. Arnold H. Glaser	1

DISTRIBUTION LIST - PROJECT GNOME
(TID - 4500(40th Ed.) Category UC - 35)

9	ABERDEEN PROVING GROUND	1	MUESER, RUTLEDGE, WENTWORTH AND JOHNSTON
1	AEROJET GENERAL CORPORATION		NASA MANNED SPACECRAFT CENTER
1	AIR FORCE INSTITUTE OF TECHNOLOGY	1	NASA SCIENTIFIC AND TECHNICAL INFORMATION FACILITY
1	AIR FORCE WEAPONS LABORATORY	2	NATIONAL AGRICULTURAL LIBRARY
1	ALBUQUERQUE OPERATIONS OFFICE		NATIONAL REACTOR TESTING STATION (PPCO)
1	ARGONNE NATIONAL LABORATORY	1	NAVAL RADIOLOGICAL DEFENSE LABORATORY
3	ARMY ENGINEER NUCLEAR CRATERING GROUP	1	NEVADA OPERATIONS OFFICE
1	ARMY ENGINEER RESEARCH AND DEVELOPMENT LABORATORIES	1	NEW YORK OPERATIONS OFFICE
6	ARMY ENGINEER WATERWAYS EXPERIMENT STATION	1	NRA, INC.
1	ARMY MATERIALS RESEARCH AGENCY	1	CAK RIDGE OPERATIONS OFFICE
2	ARMY MATERIEL COMMAND (DN-RE)	1	OFFICE OF ASSISTANT GENERAL COUNSEL FOR PATENTS (AEC)
1	ARMY MATERIEL COMMAND (NA)		OFFICE OF NAVAL RESEARCH (CODE 422)
1	ARMY MATERIEL COMMAND (RP)	1	OFFICE OF THE CHIEF OF ENGINEERS
1	ARMY NATICK LABORATORIES	7	OHIO STATE UNIVERSITY
2	ARMY NUCLEAR DEFENSE LABORATORY	1	PETROLEUM CONSULTANTS
1	ATOMIC ENERGY COMMISSION, BETHESDA	1	PHYSICS INTERNATIONAL COMPANY
1	AFC SCIENTIFIC REPRESENTATIVE, ARGENTINA	1	PICATINNY ARSENAL
1	AEC SCIENTIFIC REPRESENTATIVE, BELGIUM	1	POWER REACTOR DEVELOPMENT COMPANY
1	AEC SCIENTIFIC REPRESENTATIVE, ENGLAND	1	PUBLIC HEALTH SERVICE
1	AEC SCIENTIFIC REPRESENTATIVE, FRANCE	5	PUBLIC HEALTH SERVICE, LAS VEGAS
1	AEC SCIENTIFIC REPRESENTATIVE, JAPAN	1	PURDUE UNIVERSITY
3	ATOMIC ENERGY COMMISSION, WASHINGTON	1	RADIOPTICS, INC.
2	ATOMICS INTERNATIONAL	1	RAND CORPORATION
1	AVCO CORPORATION	1	RESEARCH ANALYSIS CORPORATION
2	BATTELLE MEMORIAL INSTITUTE	2	REYNOLDS ELECTRICAL AND ENGINEERING COMPANY, INC.
1	BATTELLE-NORTHWEST		SAN FRANCISCO OPERATIONS OFFICE
12	BEERS (ROLAND F.), INC.	5	SANDIA CORPORATION, ALBUQUERQUE
1	BEERS (ROLAND F.), INC., LAS VEGAS	4	SANDIA CORPORATION, LIVERMORE
1	BLUME (JOHN A.) AND ASSOCIATES	1	SAVANNAH RIVER OPERATIONS OFFICE
1	BROOKHAVEN NATIONAL LABORATORY	1	SCHOOL OF AEROSPACE MEDICINE
1	BUREAU OF MINES, BARTLESVILLE	1	SOUTHWEST RESEARCH INSTITUTE
1	BUREAU OF MINES, COLLEGE PARK	1	STANFORD RESEARCH INSTITUTE
1	BUREAU OF MINES, LARAMIE	1	STRATEGIC AIR COMMAND
1	BUREAU OF MINES, WASHINGTON	1	TENNESSEE VALLEY AUTHORITY
1	BUREAU OF NAVAL WEAPONS	1	UNION CARBIDE CORPORATION (ORGRP)
1	BUREAU OF SHIPS (CODE 1500)	1	UNION CARBIDE CORPORATION (ORNL)
1	DEFENSE ATOMIC SUPPORT AGENCY, LIVERMORE	4	USAF HEADQUARTERS (AFTAC)
1	DEFENSE ATOMIC SUPPORT AGENCY, SANDIA	1	U. S. COAST AND GEODETIC SURVEY, SAN FRANCISCO
1	DEFENSE ATOMIC SUPPORT AGENCY, WASHINGTON	1	U. S. GEOLOGICAL SURVEY, ALBUQUERQUE
25	DIVISION OF PEACEFUL NUCLEAR EXPLOSIVES, WASHINGTON	3	U. S. GEOLOGICAL SURVEY, DENVER
1	DU PONT COMPANY, AIKEN	2	U. S. GEOLOGICAL SURVEY, MENLO PARK
1	DU PONT COMPANY, WILMINGTON	1	U. S. GEOLOGICAL SURVEY (NOLAN)
1	EDGERTON, GERMESHAUSEN, AND GRIER, INC., LAS VEGAS	1	U. S. GEOLOGICAL SURVEY, WASHINGTON
1	FUNDAMENTAL METHODS ASSOCIATION	1	U. S. MISSION TO THE INTERNATIONAL ATOMIC ENERGY AGENCY
1	GENERAL ATOMIC DIVISION	2	U. S. WEATHER BUREAU, LAS VEGAS
1	GENERAL ELECTRIC COMPANY, CINCINNATI	1	U. S. WEATHER BUREAU, WASHINGTON
1	GENERAL ELECTRIC COMPANY, SAN JOSE	2	UNIVERSITY OF CALIFORNIA, BERKELEY
3	HAZLETON NUCLEAR SCIENCE CORPORATION	4	UNIVERSITY OF CALIFORNIA, LIVERMORE
2	HOLMES AND HARVER, INC.	1	UNIVERSITY OF CALIFORNIA, LOS ANGELES
2	LOS ALAMOS SCIENTIFIC LABORATORY	1	UNIVERSITY OF TENNESSEE (UTA)
1	LOVELACE FOUNDATION FOR MEDICAL EDUCATION AND RESEARCH	285	WHITE SANDS MISSILE RANGE
1	MOUND LABORATORY	75	DIVISION OF TECHNICAL INFORMATION EXTENSION
			CLEARINGHOUSE FOR FEDERAL SCIENTIFIC AND TECHNICAL INFORMATION